THE PLANT CELL

The Plant Cell, 2024, **00**, 1–26
https://doi.org/10.1093/plcell/koae301
Advance access publication 26 November 2024
Research Article

Maize *unstable factor for orange1* encodes a nuclear protein that affects redox accumulation during kernel development

Debamalya Chatterjee,[1] Ziru Zhang,[2] Pei-Yu Lin,[3] Po-Hao Wang,[1] Gurpreet K. Sidhu,[1] Neela H. Yennawar,[4] Jo-Wei Allison Hsieh,[3,5] Pao-Yang Chen,[3,5] Rentao Song,[2] Blake C. Meyers,[6,7] Surinder Chopra[1,*]

[1]Department of Plant Science, The Pennsylvania State University, University Park, PA 16802, USA
[2]National Center for Maize Improvement, China Agricultural University, Beijing 100083, China
[3]Institute of Plant and Microbial Biology, Academia Sinica, Nankang, Taipei 11529, Taiwan
[4]X-Ray Crystallography Facility, The Huck Institutes of the Life Sciences, The Pennsylvania State University, University Park, PA 16802, USA
[5]Genome and Systems Biology Degree Program, Academia Sinica and National Taiwan University, Taipei 10617, Taiwan
[6]The Donald Danforth Plant Science Center, St. Louis, MO 63132, USA
[7]Division of Plant Science and Technology, University of Missouri, Columbia, MO 65201, USA
*Author for correspondence: sic3@psu.edu (S.C.)
The author responsible for distribution of materials integral to the findings presented in this article in accordance with the policy described in the Instructions for Authors (https://academic.oup.com/plcell/pages/General-Instructions) is Surinder Chopra (sic3@psu.edu).

Abstract

The basal endosperm transfer layer (BETL) of the maize (*Zea mays* L.) kernel is composed of transfer cells for nutrient transport to nourish the developing kernel. To understand the spatiotemporal processes required for BETL development, we characterized 2 *unstable factor for orange1* (*Zmufo1*) mutant alleles. The BETL defects in these mutants were associated with high levels of reactive oxygen species, oxidative DNA damage, and cell death. Interestingly, antioxidant supplementation in in vitro cultured kernels alleviated the cellular defects in mutants. Transcriptome analysis of the loss-of-function *Zmufo1* allele showed differential expression of tricarboxylic acid cycle, redox homeostasis, and BETL-related genes. The basal endosperms of the mutant alleles had high levels of acetyl-CoA and elevated histone acetyltransferase activity. The BETL cell nuclei showed reduced electron-dense regions, indicating sparse heterochromatin distribution in the mutants compared with wild-type. *Zmufo1* overexpression further reduced histone methylation marks in the enhancer and gene body regions of the *pericarp color1* (*Zmp1*) reporter gene. *Zmufo1* encodes an intrinsically disordered nuclear protein with very low sequence similarity to known proteins. Yeast two-hybrid and luciferase complementation assays established that ZmUFO1 interacts with proteins that play a role in chromatin remodeling, nuclear transport, and transcriptional regulation. This study establishes the critical function of *Zmufo1* during basal endosperm development in maize kernels.

Introduction

Endosperm is the primary nutrient reservoir of maize (*Zea mays* L.) kernel. During early and mid-developmental stages endosperm undergoes intense mitotic activity, cell differentiation, cell proliferation, and endoreduplication, and forms various morphologically distinct and functionally unique cell layers (Kowles and Phillips 1985, 1988; Leroux et al. 2014; Doll et al. 2017, 2020; Dai et al. 2021; Wu et al. 2022). The entire perimeter of the endosperm is covered by a single aleurone cell layer except near phloem termini in the pedicel, where the epithelial cells differentiate into the basal endosperm transfer layer (BETL) (Olsen 2001; Dai et al. 2021). BETL is composed of an array of elongated transfer cells (BETCs) (Leroux et al. 2014). In BETCs increased plasma membrane surface area and mitochondria-rich dense cytoplasm adjacent to secondary cell wall ingrowths (CWIs) allow efficient nutrient transport from pedicel to the endosperm storage cells (Offler et al. 2003; LeClere et al. 2008; Kang et al. 2009; Leroux et al. 2014; McCurdy and Hueros 2014; Chourey and Hueros 2017). Thus, targeted manipulation of BETL development can potentially allow improvement of kernel size or nutrient quality. Studies of maize mutants such as *miniature seed1* (*Zmmn1*), *defective18* (*Zmde18*), *empty pericarp4* (*Zmemp4*), *defective kernel35* (*Zmdek35*), *pentatricopeptide repeat78* (*ppr78*), *endosperm breakdown1*(*Zmenb1*), and *dosage-effect defective kernel1*(*Zmded1*) have identified genes involved in BETL and endosperm adjacent to the scutellum (EAS) differentiation and established the importance of their proper development for nutrient accumulation in the endosperm (Gutiérrez-Marcos et al. 2007; Kang et al. 2009; Chen et al. 2017; Zhang et al. 2017; Doll et al. 2020; Wang et al. 2021). Despite these advances, our understanding of events that facilitate trans-differentiation of BETL in a spatiotemporal manner remains enigmatic. In addition to BETL, adjacent basal endosperm also comprises distinct cell layers such as conducting zone (CZ), basal intermediate zone (BIZ), embryo surrounding region (ESR), and EAS (Leroux et al. 2014; Doll et al. 2020).

The interplay among reactive oxygen species (ROS) signals, ROS-scavengers, and phytohormones can influence cell differentiation and cell death during endosperm development (Bethke and Jones 2001; Considine et al. 2003; Bailly et al. 2008; Tsukagoshi et al. 2010; Considine and Foyer 2014; Schmidt and Schippers 2015; Cheng et al. 2016; Schippers et al. 2016; Wang et al. 2017; Zeng et al. 2017; Foyer et al. 2018; Mhamdi and Van Breusegem 2018; Zhang et al. 2021). Using faba bean (*Vicia faba*) as a model, it was shown that change in hexose gradient sequentially induces auxin

Received April 17, 2024. Accepted October 17, 2024

and ethylene that activates calcium and ROS signaling leading to polarized accumulation of sterol-enriched-domain-vesicles for CWI formation in BETCs (Offler et al. 2003; Dibley et al. 2009; Zhou et al. 2010; Andriunas et al. 2013; Zhang et al. 2015, 2019a; Xia et al. 2017, 2020). In plants, ROS is produced indirectly during the TCA cycle (TCAC) and directly during lipid peroxidation, oxidoreduction, lack of antioxidants, and through mitochondrial electron-leakage (Mhamdi and Van Breusegem 2018; Suski et al. 2012). ROS also regulates the formation of 8-hydroxyguanosine (8-OHG) that affects mRNA stability, DNA damage response (DDR), and epigenetic modifications (Shen et al. 2016; Huang et al. 2019; Katsuya-Gaviria et al. 2020; Lindermayr et al. 2020). Moreover, proteins that maintain redox homeostasis also interact with chromatin remodelers and epigenetically regulate transcriptional repression and activation, precise temporal control of which is required during seed development (Engelhorn et al. 2014; Groth et al. 2016; Cho et al. 2018; Ojolo et al. 2018; Ageeva-Kieferle et al. 2019; Bellegarde et al. 2019).

The characterization of additional maize mutants with developmental defects in basal endosperm and specialized cell layers is required to decipher the function of genes and metabolites in kernel development. Maize *unstable factor for orange1* (*Zmufo1*) could be one such gene that may help understand the regulatory processes that are critical during the early stages of maize kernel development. A spontaneous dominant mutant allele *Ufo1-1* was initially identified as an epigenetic modifier of *pericarp color1* (*Zmp1*), an R2R3-MYB-transcription factor (TF) that regulates biosynthesis of orange-red phlobaphenes in the pericarp (Chopra et al. 2003). *Ufo1-1* in the presence of *P1-wr*, a functional *p1* allele, shows variable penetrance causing phlobaphenes accumulation in plant body in a small and variable subset of the progeny plants, whereas the majority of the F_1 plants revert to wild-type (WT) *P1-wr* expression (white pericarp, red cob glumes) (Chopra et al. 2003). Several mysteries associated with *Ufo1-1-* were solved by the cloning of *Zmufo1* (GRMZM2G0530177) through RNA-Seq-based k-mer analysis (Wittmeyer et al. 2018). We demonstrated that a CACTA transposable element spontaneously inserted in the first intron of *Zmufo1* drives the ectopic overexpression of *Ufo1-1* causing hyperaccumulation of phlobaphenes, growth defects, and constitutive stress-like phenotypes in the *Ufo1-1* plants (Chopra et al. 2003; Wittmeyer et al. 2018; Chatterjee et al. 2021). From *Ufo1-1*, we developed 2 stable near-isogenic lines (NILs) from *Ufo1-1* and named them "*Ufo1-1* expresser" (*U-E*) and "*Ufo1-1* silent" (*U-S*). Segregating progeny plants with WT *Zmufo1* allele were identified as WTs. We further demonstrated that the *U-E* plants had a hypomethylated CACTA in *Zmufo1* sequence and displayed characteristic *Ufo1-1* phenotypes, whereas *U-S* plants had hypermethylated CACTA and displayed WT-like phenotypes (Wittmeyer et al. 2018).

The WT (*Zmufo1*) is highly expressed in basal endosperm during 6 to 12 days after pollination (DAP) that spans through the onset of BETC formation (2 to 5 DAP) and its differentiation (4 to 12 DAP) (Talbot et al. 2002, 2007; Chen et al. 2014; Li et al. 2014; Zhan et al. 2015; Hoopes et al. 2019; Offler and Patrick 2020). *Zmufo1* and its putative orthologs are present only in some members of Poaceae family (Wittmeyer et al. 2018), which have persistent type endosperm comprised of several specialized cell layers (Becraft 2001). To further understand the role of *Zmufo1* in endosperm development, we also characterized a loss-of-function allele of *Zmufo1* with a GFP-tagged *Ds* transposon insertion in the 4th exon named *ufo1-Dsg* (Chatterjee et al. 2021).

In the current study, we show that endosperm developmental defects in *Zmufo1* mutants are associated with high ROS accumulation, oxidative DNA damage, and cell death. We also show that high ROS and differential expression of genes involved in tricarboxylic acid cycle (TCAC), redox scavenging, endosperm development, and DDR were accompanied by high levels of acetyl-CoA and histone acetyltransferase (HAT) activity. We used transmission electron microscopy (TEM) to identify the signs of chromatin changes in the basal endosperm tissue of *Zmufo1* mutants as compared with their WTs. In addition, we used *Zmp1*, the classical marker of *Ufo1-1* allele to demonstrate the effect of misregulation of *Zmufo1* on histone methylation marks. Finally, through subcellular localization of *Zmufo1* encoded intrinsically disordered protein (ZmUFO1) and identification of its interacting protein partners in a heterologous system, we further elucidate the possible molecular function of *Zmufo1*.

Results

Ufo1-1 affects sugars and plant growth in the absence of a functional *Zmp1* allele

We have previously shown that *P1-wr;Ufo1-1*-derived *U-E* NIL has an abnormal accumulation of sugar and BETL defects in the endosperm (Chatterjee et al. 2021). *U-E* (*P1-wr;Ufo1-1 Expresser*) plants appear stressed, accumulate excessive sugars in leaves, and show plant bending, twisted leaf whorls, "buggy-whip"-like phenotypes (Wittmeyer et al. 2018; Chatterjee et al. 2021). As *Ufo1-1* is also ectopically overexpressed in the pericarp, the endosperm defects observed in *U-E* plants could be the result of confounded maternal and zygotic abnormalities (Wittmeyer et al. 2018; Chatterjee et al. 2021). To address the question if abnormal phenotypes observed in *U-E* require *Ufo1-1* mediated overexpression of *p1*, we characterized *Ufo1-1* plants in the absence of a functional *p1* allele designated as *p1-ww;Ufo-1-1* (Fig. 1). *p1-ww;Ufo1-1* plants showed poor penetrance as well as growth defects such as bending and stepladder leaf phenotypes were observed similar to those *P1-wr;Ufo1-1* plants (Fig. 1A). In addition, stomata subsidiary cell defects previously shown to be associated with overexpression of *Ufo1-1* (Chatterjee et al. 2021) in *U-E* seedling leaves were also found in *p1-ww;Ufo1-1* leaves. Defective stomata in *p1-ww;Ufo1-1* leaves were 35% as compared with ~38% in *P1-wr;Ufo1-1* plants showing no notable difference (Fig. 1, B to D). Further, the *p1-ww;Ufo1-1* seedling leaves that had growth defects and high frequency of defective stomata showed increased levels of sucrose, glucose, and fructose as compared with *p1-ww* plants (Fig. 1E). Soluble sugar levels were comparable in the leaves of *p1-ww;Ufo1-1* and *P1-wr;Ufo1-1*. These results establish that *Ufo1-1* can affect various phenotypes similarly in plants carrying functional or nonfunctional *Zmp1* alleles. However, for further studies, we used the functional *Zmp1* as a reporter because of the accumulation of phlobaphenes and the ease to identify any silent individuals from *U-E* to *U-S*.

To further distinguish between the direct effects of *Ufo1-1* from those of *p1* overexpression, we reanalyzed the publicly available 14 DAP *P1-rr* pericarp transcriptome data (Morohashi et al. 2012). Parametric analysis of gene set enrichment (PAGE) from *U-E* (Wittmeyer et al. 2018; Chatterjee et al. 2021) and *P1-rr* (Morohashi et al. 2012) transcriptomes revealed both similar as well as unique Gene Ontologies (GO) (Supplementary Table S1). Both the transcriptomes have upregulated GO terms for "flavonoid biosynthesis" and phenylpropanoid metabolism, whereas downregulation of DNA replication. However, GO terms related to ribosome biogenesis and nucleolus were downregulated in *Ufo1-1* 18 DAP pericarp transcriptome but upregulated in 14 DAP *P1-rr* pericarp transcriptome (Supplementary Table S1).

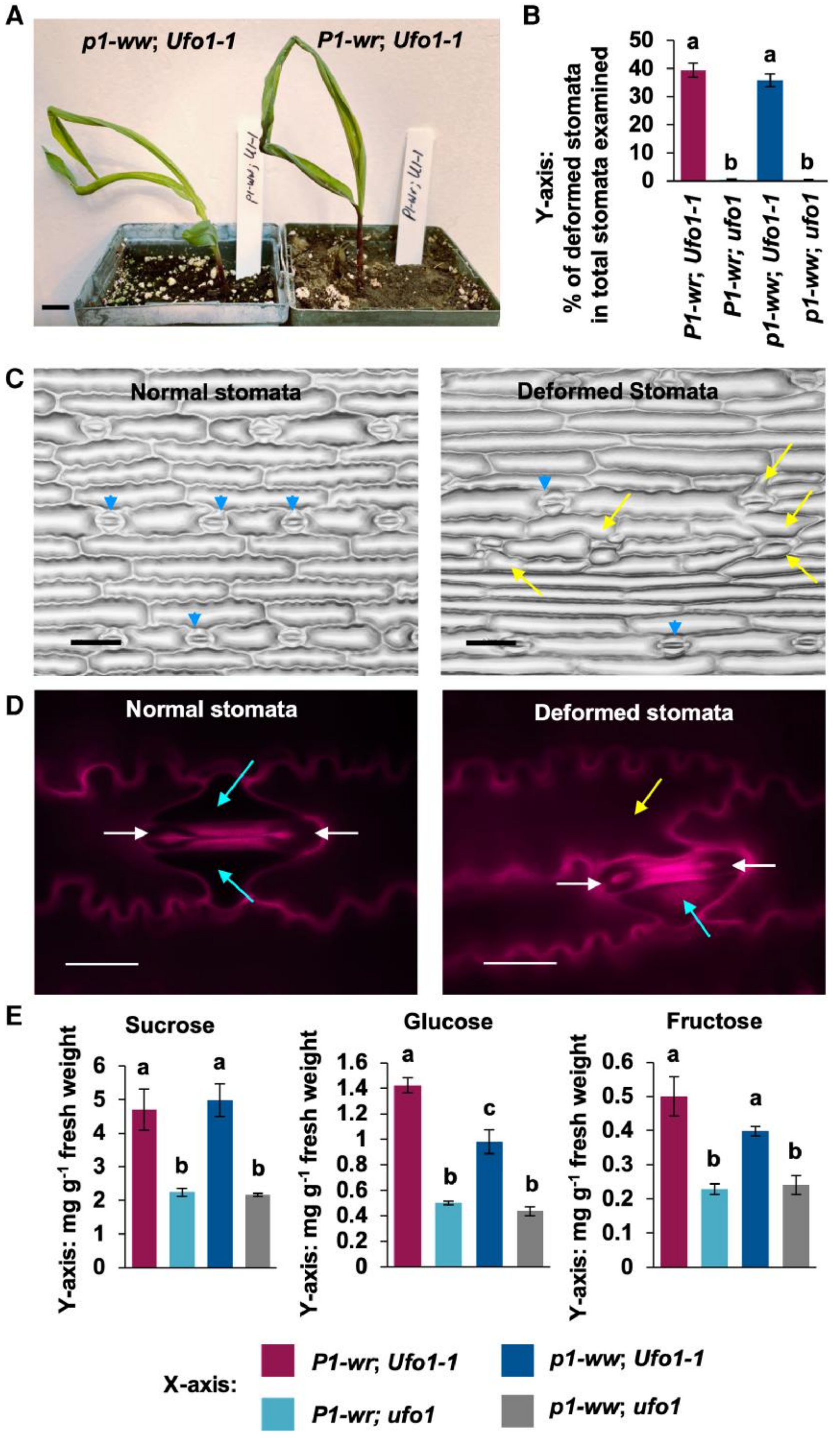

Figure 1. *Ufo1-1* affects stomata development and soluble sugar content in leaves in the absence of a functional *pericarp color1* allele. **A)** Representative image of *p1-ww*;*Ufo1-1* and *p1-wr*;*Ufo1-1* plants showing bending and stepladder phenotypes. Scale bar = 15 mm. **B)** Percentage of stomata defects out of all stomata examined. **C)** Light micrographs of *U-E* abaxial leaf epidermal impression showing normal and defective stomata. Scale bar = 0.6 mm. **D)** Epifluorescence micrographs of normal and defective stomata captured using propidium iodide staining of leaf abaxial epidermal peels from the fully opened youngest leaf of (vegetative growth stage 2) V3 plants. Scale bar = 20 mm. **E)** Levels of soluble sugars (sucrose, glucose, and fructose) in the fully opened youngest leaf of V3 plants. All bar diagrams shown are mean ± SE (standard error). Different letters indicate significance at $P \leq 0.05$ using one-way ANOVA with post-hoc Tukey's HSD test. A total of 3 biological replicates were used each comprising 10 plants. *P1-wr*;*ufo1* and *p1-ww*;*ufo1* were used as wild-type controls for *P1-wr*;*Ufo1-1* and *p1-ww*;*Ufo1-1* plants, respectively. White, cyan, and yellow arrow indicates stomata guard cell, normal, and defective subsidiary cells, respectively. Blue arrowhead indicates normal stomata.

Thus, based on these above results, a synergistic effect of the overexpression of both *Zmufo1* and *Zmp1* on gene expression changes in the transcriptome of *U-E* plants leading to several defective phenotypes cannot be ruled out. Further work will be needed to develop *p1-ww;U-E* and *p1-ww;U-S* NILs to address the question of the role of *p1* overexpression in various defects observed in *U-E* plants. However, the study of the *ufo1-Dsg* that is devoid of abnormal *Zmp1* expression helps us to decipher the direct role of *Zmufo1*.

Mutations in *Zmufo1* affect the expression of basal endosperm marker genes

We used NILs developed from *P1-wr*; *Ufo1-1* (*U-E* and *U-S*) as well as *ufo1-Dsg* loss-of-function allele (Fig. 2). The 10 DAP old *U-E* kernels had ∼7.2-fold higher expression of *Ufo1-1*, with abnormal basal endosperm, altered accumulation of sugar, starch, and hormone as well as small seed size, lower seed weight, and signs of developmental delay than that of WT (Chatterjee et al. 2021; Fig. 2A). The *ufo1-Dsg* also had reduced seed weight, abnormal sugar, starch, and hormone accumulation as well as BETL cellular defects as compared with W22 WT plants. Although both the gain-of-function (*U-E*) and loss-of-function (*ufo1-Dsg*) had loosely organized cell layers between placentochalaza (PC) and BETL region, the BETL defects were not identical between them.

We used light microscopy to investigate endosperm differentiation of the 7 DAP *U-E* and *ufo1-Dsg* seeds (Fig. 2B). Seeds of *U-E* and *ufo1-Dsg* showed a substantial remnant of nucellus between the pericarp and endosperm as well as a small size of endosperm compared with that of *U-S*, WT, and W22. This result corroborates our previous findings of retention of nucellus at 10 DAP *U-E* and *ufo1-Dsg* seeds (Chatterjee et al. 2021). Together these results indicate a delay in *U-E* and *ufo1-Dsg* kernel development. Scanning electron microscopy (SEM) revealed that *U-E* BETCs were cuboidal, shorter flange-type, and lacked reticulate CWIs (Fig. 2C). Whereas *ufo1-Dsg* BETCs were smaller than that of WT cells, had a prevalence of reticulate CWIs, and lacked flange-type CWIs. The *U-S* kernels had normal BETCs similar to those in WT (Fig. 2C).

Next, we tested expression patterns of BETL-specific markers *myb-related protein1* (*Zmmrp1*), *basal endosperm transfer layer1* (*Zmbetl1*), *basal endosperm transfer layer2* (*Zmbetl2*), *miniature seed1* (*Zmmn1*), *transfer cell response regulator1* (*Zmtcrr1*), and *sugars will eventually be exported transporter4c* (*Zmsweet4c*) in basal endosperms dissected from 10 DAP kernels (Fig. 2D). The master regulator *Zmmrp1* and downstream marker genes except were downregulated in *ufo1-DsG* as compared with W22. However, all the marker genes except *Zmmn1* and *Zmmrp1* were highly expressed in *U-E* as compared with WT and *U-S* representing an aberrant expression pattern as compared with that in *ufo1-DsG*. Although, in *U-E*, there was high ectopic expression of *aleurone9* (*Zmal9*), an aleurone marker, but as expected, this gene did not show any expression change in *ufo1-DsG* compared with W22. We further analyzed BETL, CZ, and ESR cells in 10 DAP kernels of *proBETL1::GUS* transgenic plants introgressed in *U-E* and *ufo1-Dsg* alleles. The *proBETL1::GUS;U-E* transgenic plants showed increased GUS activity in BETL and CZ as compared with control kernels of *proBETL1::GUS;* WT plants (Fig. 2, E and F). The GUS staining in *proBETL1::GUS;ufo1-Dsg* kernels was very low in BETL and CZ but relatively high in the ESR region. These results indicate that misregulation of *Zmufo1* not only affects the expression levels but may also alter the spatial expression pattern of BETL-marker genes.

Zmufo1 mutants have abnormal raffinose, ROS, and cell death

Our previous studies showed that leaves of *U-E* plants produce photoinduced lesions with abnormal accumulation of sucrose and H_2O_2 (Wittmeyer et al. 2018; Chatterjee et al. 2021). As raffinose is induced by sucrose as well as ROS and is considered a marker of oxidative stress, we quantified it in *Zmufo1* mutants (Supplementary Fig. S1; Panikulangara et al. 2004; Nishizawa-Yokoi et al. 2008; Sengupta et al. 2015). Raffinose was ∼2-fold higher in 24 DAP and mature dry kernels of *U-E*, as compared with *U-S* and WT. However, in *ufo1-Dsg*, 24 DAP and mature dry kernels had reduced raffinose content as compared with W22. We did not detect raffinose at any stage earlier than 24 DAP kernels of mutants. Based on these results, we hypothesized that oxidative stress could be one of the underlying causes of the developmental defects in *Zmufo1* mutants.

Next, we investigated if the BETL defects in *U-E* and *ufo1-Dsg* kernels could be associated with altered ROS levels. Incubation in nitroblue tetrazolium chloride (NBT) (Fig. 3; Supplementary Fig. S2) showed high superoxide in aleurones of 7 DAP kernels, whereas 10 and 16 DAP kernels had strong NBT staining in the basal endosperm of both mutants as compared with their WT (Fig. 3A). The 3,3′-diaminobenzidine (DAB) staining for H_2O_2 was high in 7, 10, and 16 DAP whole endosperm of both mutants (Supplementary Fig. S2). Quantification in 10 DAP kernels showed ∼3.5 times higher H_2O_2 levels in *U-E* than in WT and ∼3.8 times higher H_2O_2 in *ufo1-Dsg* than in W22 (Fig. 3B). *U-S* did not show any significant difference in H_2O_2 levels at 10 DAP kernel as compared with WT.

ROS react with DNA, proteins, and lipids causing cytotoxicity and cell death (Mittler et al. 2011). To investigate if ROS accumulation caused fragmentation of nuclear DNA and cell death in the basal endosperm region of 10 DAP kernels, terminal deoxynucleotidyl transferase dUTP nick-end labeling (TUNEL) assay (Lozano et al. 2009) was performed (Fig. 3C). The basal endosperm region comprising PC, BETL, and CZ in mock-treated *U-E* and *ufo1-Dsg* had 4.3-fold and 8.6-fold more cells displaying TUNEL-positive nuclei, respectively as compared with their WT controls (Fig. 3D). Whereas, *U-S* had a mean of 58 TUNEL-positive nuclei per field of view (FOV) that was statistically similar to the number observed in WT.

As TUNEL is not a direct test for oxidative DNA damage, we performed the 8-hydroxy-2′-deoxyguanosine (8-OHdG) colorimetric assay using 10 DAP kernels. The 8-OHdG assay showed an increase of oxidative DNA damage in both *Zmufo1* mutants compared with their respective WTs and *U-S*. However, the level of DNA damage in *ufo1-Dsg* (0.0483% of total DNA) was lower than that of *U-E* (0.0766% of total DNA) (Fig. 3E). Since young root tips are prone to DNA damage, an 8-OHdG assay was also performed in root tips from seedlings 5 days after germination (DAG). High oxidative DNA damage was observed in *U-E* root tips possibly due to ectopic overexpression of *Zmufo1* (Fig. 3E). Using reverse transcription quantitative PCR (RT-qPCR), we assayed the expression of 4 genes, *breast cancer susceptibility gene1* (*Zmbrca1*), *radiation sensitive 51a* (*Zmrad51a*), *lupus ku autoantigen protein p70* (*Zmku70*), and *lupus ku autoantigen protein p80* (*Zmku80*), that are markers of oxidative stress and DDR in 10 DAP basal endosperm (Fig. 3F). *Zmbraca1* had lower expression in both *U-E* and *ufo1-Dsg* than their respective WTs. Although *Zmrad51a*, *Zmku70*, and *Zmku80* showed notable upregulation in *U-E* than WT, differential expression was not observed between *ufo1-Dsg* and W22. Only, *Zmku70* had significant downregulation in *ufo1-Dsg* than W22.

Antioxidant supplementation alleviates kernel defects of *Zmufo1* mutants

A direct test was performed to investigate if abnormal ROS accumulation is associated with developmental defects in *U-E* and *ufo1-Dsg* kernels. Developing kernels were in vitro cultured for 12 d in ½ Murashige and Skoog (MS) media with and without 1 mM glutathione (GSH) and 1 mM ascorbic acid (AsA) (Dietz et al. 2016; Fig. 4; Supplementary Fig. S3). Exposing the 10 DAP kernels of *ufo1-Dsg* and *U-E* to antioxidants reduced ROS accumulation and alleviated the defects, as evident from NBT staining and

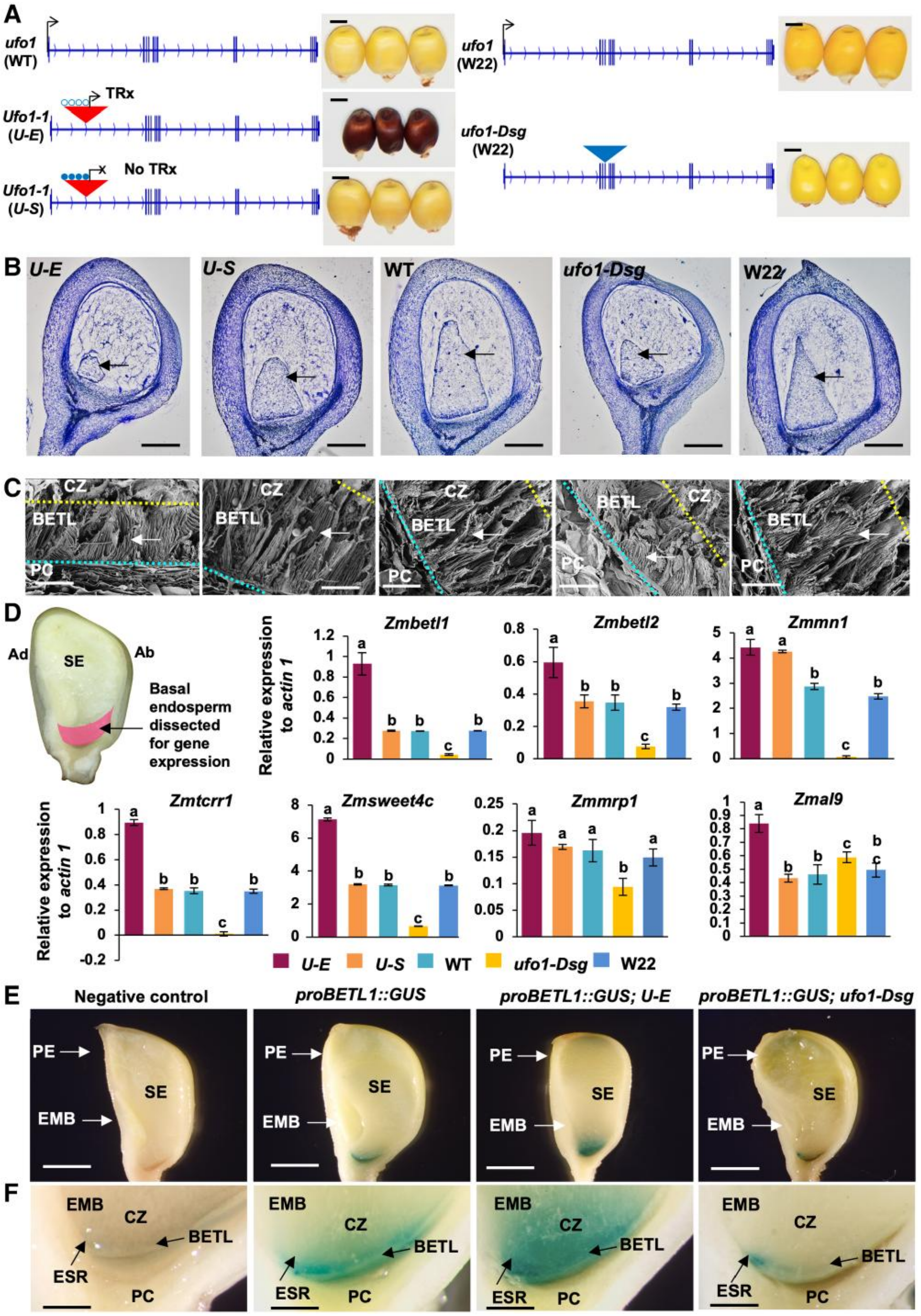

Figure 2. *Zmufo1* mutants have defective basal endosperm. **A)** Line diagram depicts different *ufo1* alleles, seed phenotypes, and basal endosperm transfer layer (BETL) defects. Short vertical lines along the horizontal line indicate exons and small blue arrowheads indicate the direction of transcription. Black bent arrows indicate the transcription start sites. Red and blue triangles indicate *CACTA* and *Dsg* transposon insertion, respectively. Empty and filled blue circles represent cytosine DNA hypo and hyper-methylation respectively. TRx indicates transcription. **B)** Light micrographs of 7 days after pollination (DAP) kernel sections stained with toluidine blue O. *U-E* and *ufo1-Dsg* have smaller endosperm indicating delayed development. The *U*-S, WT, and W22 have normal development. Black arrows indicate endosperm. Scale bar = 1 mm. **C)** Scanning electron micrographs showing BETL cells from 10 DAP kernels. Cyan dotted lines mark the BETL-placentochalaza interface and yellow dotted lines mark BETL-conducting zone interface. The white arrows point to cell wall ingrowths of TCs. Scale bar = 10 *μ*m. **D)** Ten DAP kernel cartoon shows the basal endosperm region dissected for RT-qPCR assays of BETL-specific and functionally related genes. Results shown are mean ± SE. A total of 30 independent kernels comprising 10 kernels from 3 independent ears were used. Different letters indicate significance at $P \leq 0.05$ using one-way ANOVA with post-hoc Tukey's HSD test. **E** and **F)** Histochemical staining for β-glucuronidase (GUS) in 10 DAP kernels of *Zmbetl1 promoter::GUS* plants. GUS staining in the dissected half of kernel **E)** and a close-up of the basal endosperm **F)**. In panels **E** and **F)**, negative control represents genetic background and a nontransgenic segregant. Different genotypes are: *proBETL1::GUS* is a positive control, *proBETL1::GUS;U-E* and *proBETL1::GUS;ufo1-Dsg* are introgression lines. Scale bar = 0.15 mm. Images represent at least 10 kernels from independent ears of individual plants per genotype. PC, placentochalaza; PE, pericarp; SE, starchy endosperm; EMB, embryo; ESR, embryo surrounding region; CZ, conducting zone.

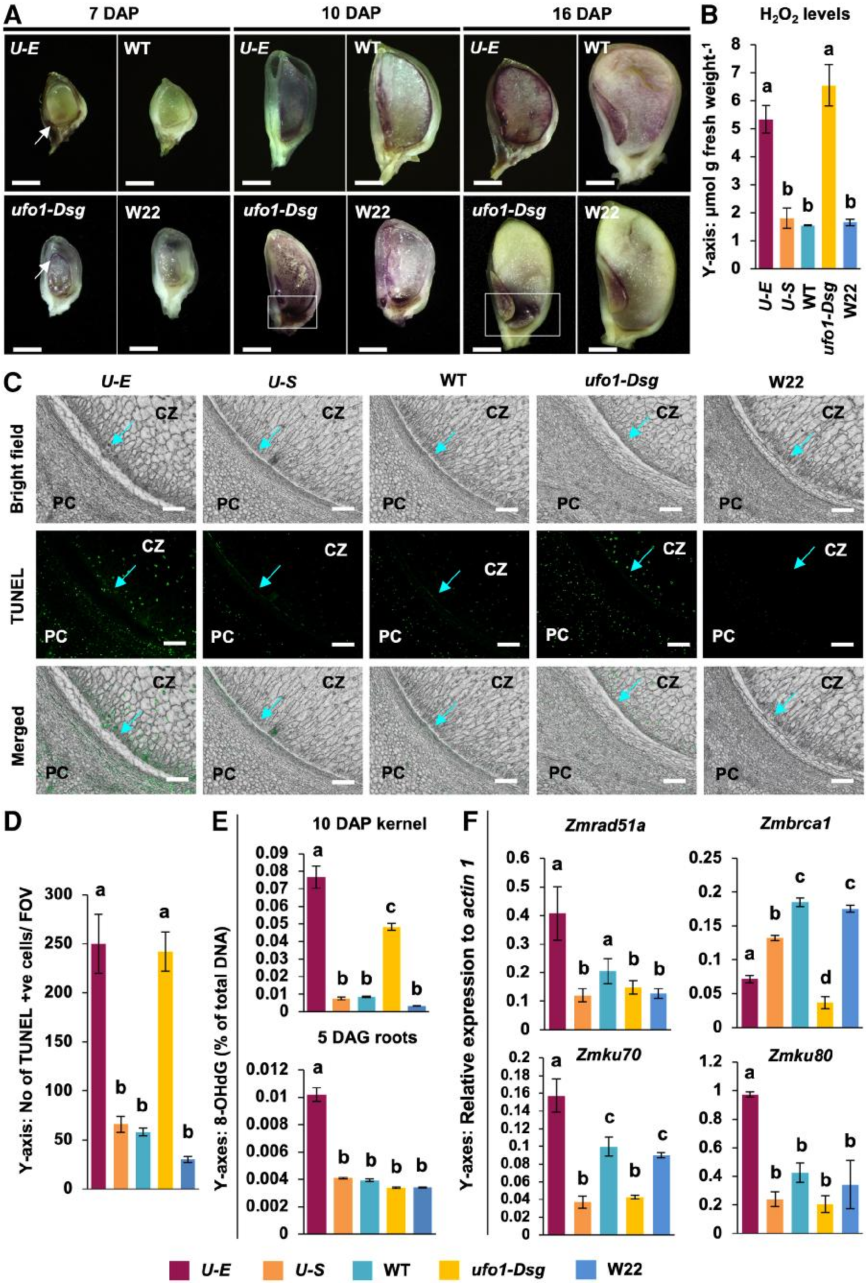

Figure 3. Abnormal reactive oxygen species accumulation, cell death, and DNA damage defects in *Zmufo1* mutants. **A)** ROS accumulation assay using nitroblue tetrazolium (NBT) dye in 7, 10, and 16 DAP kernels of different genotypes as shown. The result indicates high NBT staining at the basal region of *U-E* and aleurone of *ufo1-Dsg* kernels at 7 DAP as compared with their respective wild-types. At 10 and 16 DAP, *U-E* kernel shows high NBT staining throughout the endosperm, and *ufo1-Dsg* kernel shows very intense staining at the basal endosperm region as compared with their wild-types. Scale bar = 0.15 mm. White arrows and rectangles indicate areas with high NBT staining. Fifteen kernels per ear from 3 independent ears were used for each genotype and each timepoint. **B)** Quantification of H_2O_2 showing higher levels in *U-E* and *ufo1-Dsg* 10 DAP kernels as compared with *U-S* and their respective wild-types. **C** and **D)** Terminal deoxynucleotidyl transferase dUTP nick-end labeling (TUNEL) of 10 DAP kernels. Fluorescein labeling of the TUNEL-positive nuclei seen as green dots. Cyan arrows indicate the nucleus stained by TUNEL in the basal endosperm transfer layer. The number of TUNEL +ve cells per field of view (FOV). **E)** Oxidative DNA damage in 10 DAP kernels and 5 days after germination (DAG) root tips of mutants and wild-type controls detected as the level of 8-hydroxy-2′-deoxyguanosine (8-OHdG) and expressed as the percentage of total DNA ($n = 3$ biologically independent plants). **F)** Expression of DNA damage response marker genes in 10 DAP kernels using RT-qPCR. Statistical analyses described below apply to all statistical analyses in this figure. The results shown are mean ± SE. A total of 45 independent kernels comprising 15 kernels from 3 independent ears were used. Letters indicate significance at $P \leq 0.05$ using one-way ANOVA with post-hoc Tukey's HSD test.

biomass of kernels subjected to antioxidants (GSH and AsA) supplementation compared with mock treatment (Fig. 4, A to C). By contrast, the antioxidant-treated *U-S*, WT, and W22 kernels showed a slight reduction in the size and biomass compared with the mock (Fig. 4, B and C). In the antioxidant-supplemented *U-E* and *ufo1-Dsg* kernels, soluble sugars (D-glucose, D-fructose, and sucrose) showed a reversion to normal accumulation compared with the mock kernels (Fig. 4D).

There was also a reduction in the intensity of oxidative DNA damage in antioxidant-treated *U-E* and *ufo1-Dsg* kernels as compared with mocks (Fig. 4E). The colorimetric 8-OHdG assay showed less DNA damage in antioxidant-treated *U-E* and

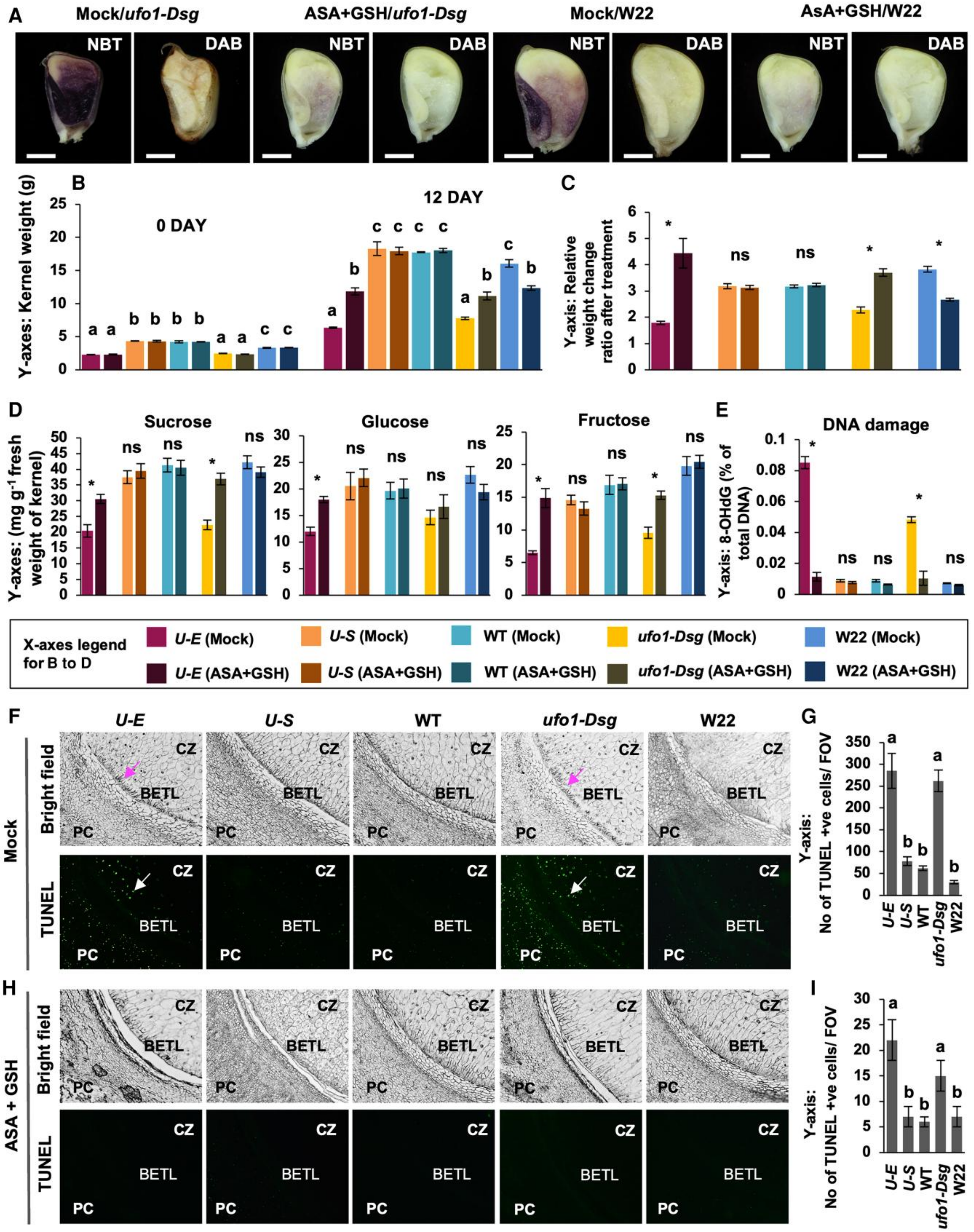

Figure 4. Effects of exogenous antioxidant in vitro treatment on the kernel phenotype of *Zmufo1* mutants. **A)** NBT staining, **B)** biomass, and **C)** relative biomass changes (ratio of antioxidant to mock) of the 10 days after pollination (DAP) kernels at the 0th and 12th days of culture in mock and antioxidant-supplemented MS media (1 mM glutathione [GSH] and 1 mM ascorbic acid [AsA]). **D)** Quantification of soluble sugars (sucrose, glucose, and fructose) in mock and antioxidant-supplemented kernels. **E)** Oxidative DNA damage detected as the level of 8-hydroxy-2′-deoxyguanosine (8-OHdG) and expressed as a percentage of total DNA. **F** to **I**) Terminal deoxynucleotidyl transferase dUTP nick-end labeling (TUNEL) signal **F, H)** and no of TUNEL +ve cells field of view (FOV) **G, I)** in the basal endosperm of mock and antioxidant-treated kernels **F, G)** versus antioxidant-supplemented media **H, I)**. Magenta and white arrows indicate defective BETL and TUNEL signals, respectively. Different genotypes are shown below the **D)** panel. Statistical analyses described below apply to all statistical analyses in this figure. Results shown are mean ± SE. A total of 30 independent kernels comprising 10 kernels from 3 independent ears were used. Asterisks (*) and "ns" indicate significance at $P \leq 0.05$ and nonsignificant, respectively, using Student's *t*-test.

ufo1-Dsg kernels (Fig. 4E). To confirm if ROS accumulation contributed to the DNA damage-induced cell death, a TUNEL assay of basal endosperm was performed on kernels cultured with and without antioxidant supplementation (Fig. 4, F to I). The basal endosperm region (PC, BETL, and CZ) in mock-treated *U-E* and *ufo1-Dsg* had 4.6-fold and 8.7-fold more cells displaying TUNEL-positive nuclei, respectively, as compared with their corresponding WT controls. Whereas, *U-S* had a mean of 78 TUNEL-positive nuclei per FOV which was statistically similar to the number of TUNEL-positive nuclei observed in WT. Interestingly, antioxidant supplementation noticeably reduced the number of TUNEL-positive nuclei in all genotypes. Although *U-E* still had 3.7-fold more TUNEL-positive nuclei per FOV as compared with that of antioxidant-treated WT, it was 13-fold less as compared with that of mock-treated *U-E* kernels. A similar trend was observed for antioxidant-treated *ufo1-Dsg* that had a notable reduction of the number of mean TUNEL-positive nuclei per FOV than that of mock-treated *ufo1-Dsg* kernels.

To detect if antioxidant-supplemented alleviation of ROS had any reversible effect on gene expression, RT-qPCR was performed for several ROS- and BETL-marker genes (Supplementary Fig. S4). The ROS-marker genes, especially *alternative oxidase2* (*Zmaox2*), *catalase1* (*Zmcat1*), *superoxide dismutase4A* (*Zmsod4A*), *ascorbate peroxidase4* (*Zmapx4*), and *guaiacol peroxidase2* (*Zmpox2*) had higher expression in *U-E* and *ufo1-Dsg* mock kernels than their WTs. Compared with mock kernels, GSH and AsA-supplemented kernels showed reduced expression of all 8 ROS genes tested in all genotypes. Interestingly, the 3 BETL-marker genes were reversibly affected in antioxidant-treated kernels as compared with mock kernels; *U-E* had reduced expression, while *ufo1-Dsg* showed increased expression of these genes in antioxidant-treated kernels. The antioxidant-treated WT kernels also showed some expression reduction of all 3 BETL genes. The *U-S* and W22 kernels did not show any notable expression changes of *Zmbetl2* and *Zmbetl1*, respectively, upon antioxidant supplementation. Interestingly, no notable change in *Zmufo1* gene expression was observed in antioxidant-treated kernels, indicating that *Zmufo1* may not be transcriptionally modulated by ROS levels (Supplementary Fig. S3).

Misregulation of *Zmufo1* affects the transcription of functionally diverse groups of genes

To understand the cause of abnormal ROS accumulation in the endosperm, we performed RNA-Seq of 10 DAP *ufo1-Dsg* kernels and identified significant differentially expressed genes (DEGs) (P-adj-value ≤ 0.05 and $\log_2$fold change ≥ 1.5) (Fig. 5; Supplementary Fig. S4; Supplementary Data Set 1). A total of 109 and 99 genes were up- and downregulated in *ufo1-Dsg*, respectively, as compared with W22. The major downregulated GO terms were "carboxylic acid", "macromolecule metabolic process", "autophagy", and multiple autophagy-related terms. Upregulation of GO terms "TOR signaling", "regulation of cell size" in *ufo1-dsg* transcriptome, as well as increased programmed cell death in 10 DAP kernels of *ufo1-Dsg* (Fig. 3, B and C) was consistent with downregulation of "autophagy" due to their antagonism (Neufeld 2010; Pu et al. 2017; Robin et al. 2019).

Rate-limiting genes of the TCAC such as *succinate dehydrogenase 11* (*Zmsudh11*), *isocitrate dehydrogenase*, and *2-oxoglutarate dehydrogenase E1* were downregulated in *ufo1-Dsg* (Fig. 5). ROS quenchers such as cytosolic *ascorbate peroxidase5* and *glutathione S-transferase18* (*Zmgst18*) were upregulated in *ufo1-Dsg* (Fig. 5; Supplementary Data Set 1). Moreover, genes crucial for BETL and ESR development, biosynthesis of xyloglucan and arabinogalactan, metabolism and signaling of sphingolipid and sterol, translational regulation, posttranslational modification, and protein recycling, ribosome biogenesis, as well as TFs involved in the hormonal response, regulation of cell fate, cell wall biosynthesis, and polycomb repressive complex2 (PRC2)-related genes were differentially expressed in *ufo1-Dsg* transcriptome (Fig. 5).

The diverse category of DEGs identified from the *ufo1-Dsg* kernel transcriptome was also observed previously in the *U-E* 18 DAP pericarp transcriptome (Wittmeyer et al. 2018; Chatterjee et al. 2021). Basal endosperm-specific genes such as *Zmbetl2*, *basal endosperm transfer layer3* (*Zmbetl3*), *basal endosperm transfer layer9* (*Zmbetl9*), *bHLH-transcription factor 175* (*Zmbhlh175*), and *Zmmn1* were upregulated in 18 DAP *U-E* pericarp as compared with that of WT but were downregulated in *ufo1-Dsg* 10 DAP kernel as compared with that of W22 (Supplementary Fig. S4). RT-qPCR assay of the 10 DAP basal endosperm also showed upregulation of *Zmbetl1*, *Zmbetl2*, and *Zmmn1* in *U-E* but their downregulation in *ufo1-Dsg* as compared with respective WT controls (Fig. 2D). DEGs in previously generated *U-E* transcriptomes from 18 DAP pericarp and V10 leaf also correspond to GO terms "oxidoreductase activity", "biosynthesis of secondary metabolites", "phenylpropanoid biosynthesis", "oxidative stress", "NAD(P)H oxidase H_2O_2-forming activity", and "peroxidase activity" (Supplementary Fig. S4). RT-qPCR assay (Fig. 5B) further confirmed differential expression of *succinate dehydrogenase11* (*Zmsudh11*), *glutathione transferase18* (*Zmgst18*), *fertilization independent endosperm1* (*Zmfie1*), *HMG-transcription factor 3* (*Zmhmg103*), and a PPIase (*cyclophilin-like peptidyl-prolyl cis-trans isomerase*, *Zm00001d050635*) in basal endosperm of 10 DAP kernels of *U-E*, *U-S*, and *ufo1-Dsg* as compared with their respective WT controls.

Abnormal acetyl-CoA and HAT activity in *ufo1-Dsg* and *U-E*

Abnormal ROS accumulation in *U-E* and *ufo1-Dsg* kernel as well as altered expression of TCAC genes in the transcriptomes of both the mutants prompted us to quantify acetyl-CoA in the basal endosperm (Fig. 6). In *U-E* kernels at 10 DAP, basal endosperm had significantly high (~9 pmol mg^{-1}) acetyl-CoA as compared with all other alleles (~6 to 6.5 pmol mg^{-1}) (Fig. 6A). At 12 and 18 DAP, both *U-E* and *ufo1-Dsg* had notably higher levels of acetyl-CoA as compared with their respective WT controls and *U-S* (Fig. 6A).

High level of cytosolic acetyl-CoA induces histone acetylation (Galdieri and Vancura 2012; Chen et al. 2017a), thus we quantified HAT activity in the basal endosperm tissue of *U-E*, *U-S*, *ufo1-Dsg*, and their respective WT controls (Fig. 6B). Basal endosperms from 10, 12, and 18 DAP *U-E* kernels had 1.6, 3.3, and 5.1-fold higher HAT activity, respectively, as compared with that of WT. The *ufo1-Dsg* also had 1.3, 2.3, and 4.5-fold higher HAT activity in basal endosperms obtained from 10, 12, and 18 DAP kernels, respectively, as compared with that of W22. The HAT activity in *U-S* was similar to that of WT at all 3 time points. Together, these results established high levels of acetyl-CoA and HAT activity in *U-E* and *ufo1-dsg* as compared with their respective WT controls.

Abnormal features of nuclei, nucleoli, and chromatin of *Zmufo1* mutants

Increased HAT activity in basal endoderm of *Zmufo1* mutants prompted us to directly observe any changes in the nuclear structure. The abnormal development of maize endosperm has also been observed in *reas1* mutant and has been associated with altered nuclear structures (Qi et al. 2016). We used TEM to observe

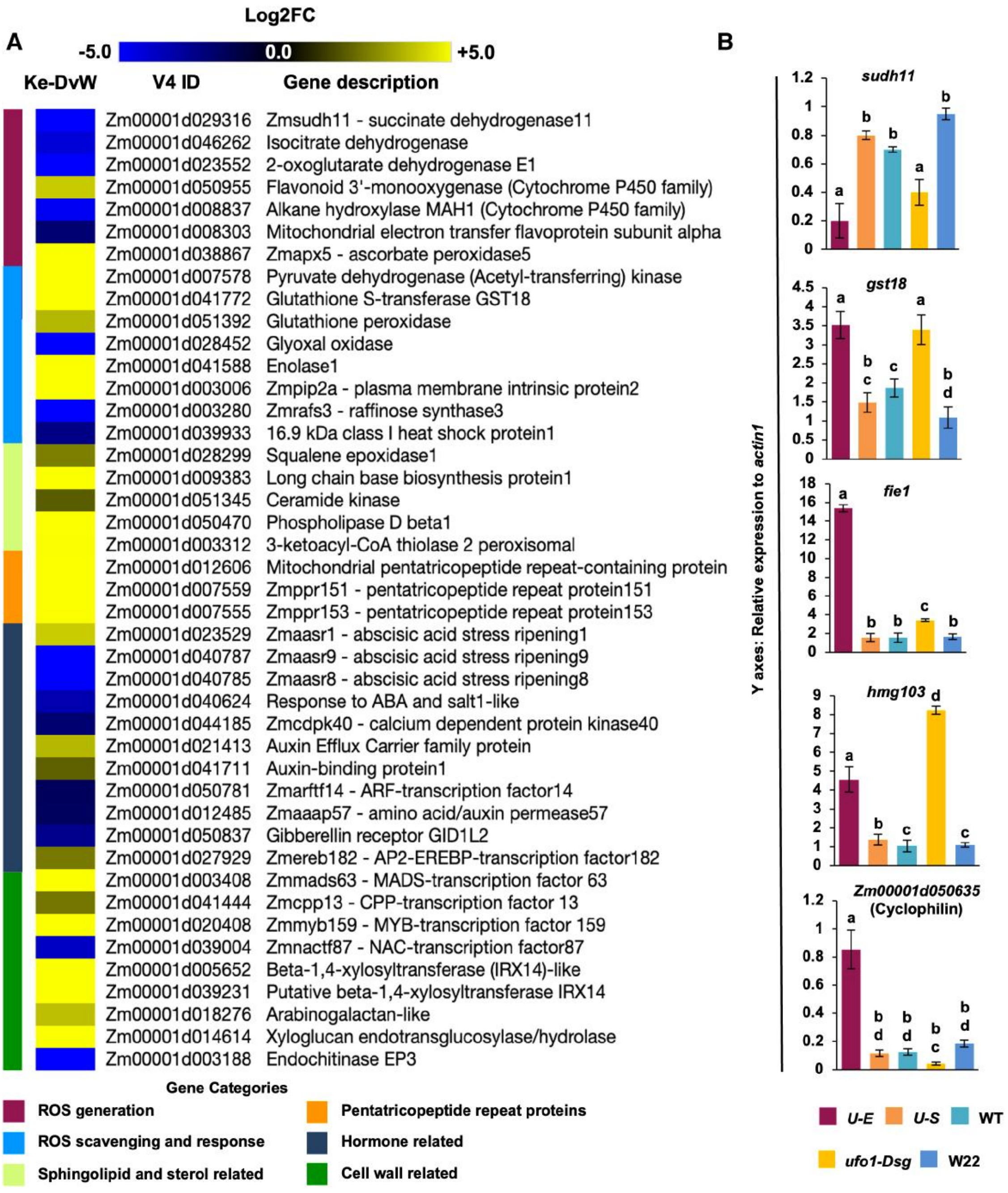

Figure 5. Significant differentially expressed genes of *ufo1-Dsg* kernel transcriptome. **A)** Heatmap depicting the $\log_2$fold change of differentially expressed genes (DEGs) involved in redox homeostasis from 10 DAP kernel of *ufo1-Dsg* as compared with that of W22 (wild-type) (Ke-DvW). Two biological replicates of *ufo1-Dsg* kernels were used to generate the transcriptome data. The description indicates gene name (with "Zm" prefix) designated by MaizeGDB (https://www.maizegdb.org) or protein name or identified protein domain. **B)** Expression of selected genes in the basal endosperm of 10 days after pollination (DAP) kernels of the *Zmufo1* mutants detected using RT-qPCR. The results shown in the bar graphs are mean ± SE. A total of 30 independent kernels comprising 10 kernels from 3 independent ears were used. Different letters indicate significance at $P \leq 0.05$ using one-way ANOVA with post-hoc Tukey's HSD test.

the nuclei of CZ cells because these are less complex as compared with BETCs (Fig. 6C). In *U-E* and *ufo1-Dsg*, CZ cells had reduced accumulation of starch granules and protein bodies compared with their WTs (Fig. 6D). Further, *U-E* had 68% of the observed cells with large nucleoli (% of nucleolar size/nuclear size = 15), whereas *U-S* and WT had relatively smaller normal nucleoli (% of nucleolar size/nuclear size = 10) in 93% and 90% cells, respectively. The 3 nucleolar components, the fibrillar centers, the dense fibrillar component, and the granular component, were distinctly identifiable in the SE cells of WT, *U-S*, and W22 in higher magnification micrographs (Kalinina et al. 2018; Fig. 6E). Electron-dense regions (EDRs) in TEM micrographs are classically used to identify heterochromatin that represents morphologically distinct condensed chromatin enriched for suppressive marks such as H3K9/27me3 (Davies 1968; Cmarko et al. 2003; Rübe et al. 2011; Wenzel et al. 2011). We observed 5 to 7 large (>0.2 mm) EDRs in the nucleus of all 20 observed cells in each of WT, *U-S,* and W22. In contrast, among the 20 observed cells of each genotype, 75% of *U-E* and 80% of *ufo1-Dsg* cells had zero to 3

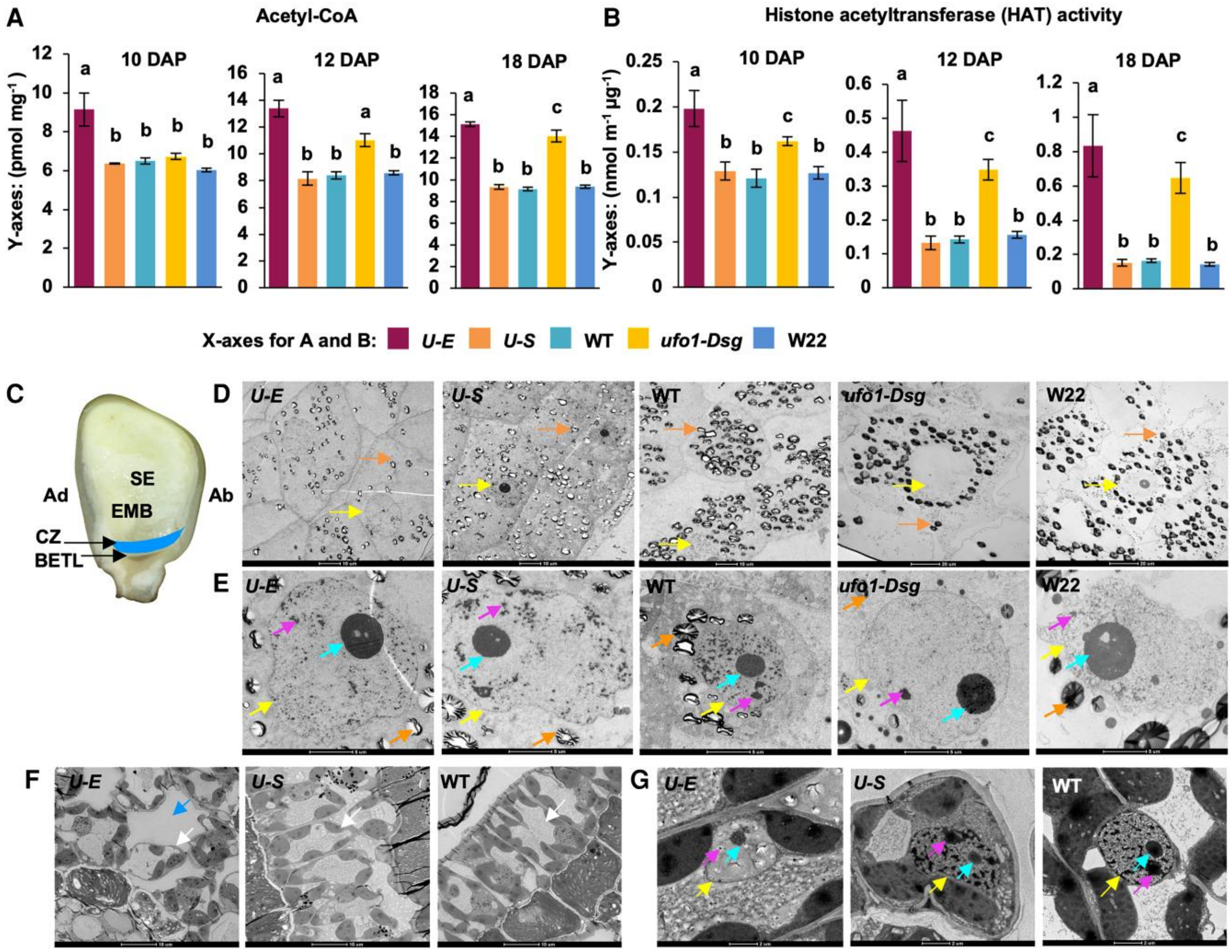

Figure 6. Misregulation of *Zmufo1* affects the acetyl-CoA accumulation, histone acetyltransferase activity, and the distribution of electron-dense regions in the nucleus. **A)** Acetyl-CoA quantification. **B)** Quantification of histone acetyltransferase (HAT) activity. **C)** A cartoon showing the conducting zone (CZ) interface region used for transmission electron microscopy (TEM) presented in **D** to **G)**. BETL, basal endosperm transfer layer; EMB, embryo; Ad, adaxial; Ab, abaxial. **D)** Abnormal accumulation of starch and protein bodies in the cells of CZ-SE region in 15 DAP kernels of *Zmufo1* mutants. **E)** Abnormal nuclear features of *Zmufo1* mutants in CZ-SE interface cells. *U-E* and *ufo1-Dsg* nucleus showing reduced electron-dense regions (EDRs) compared with respective wild-type controls. **F)** Micrographs of cross-sections of abnormal *U-E* leaves show atypical development and organization of spongy mesophyll parenchyma in *U-E* as compared with normal leaves of *U-S* and WT. **G)** Representative *U-E* nucleus showing reduced EDRs compared with *U-S* and respective wild-type control. Orange, yellow, magenta, cyan, white, and blue arrows indicate starch granules, nucleus, EDRs, nucleolus, mesophyll cells, abnormal space among cells, respectively. Scale bars = **D, F)** 10 μm; **E)** 5 μm; and **G)** 2 μm. Statistical analyses described below apply to all statistical analyses in this figure. The results shown in the bar graphs are mean ± SE. A total of 30 independent kernels comprising 10 kernels from 3 independent ears were used. Different letters indicate significance at $P \leq 0.05$ using one-way ANOVA with post-hoc Tukey's HSD test.

large EDRs but small electron-dense puncta (<0.2 mm) spread throughout the nucleus (Fig. 6E). *U-E* cells also had asymmetric mesophyll parenchyma organization resembling maize *crinkly4* (Becraft et al. 2001; Chatterjee et al. 2021; Fig. 6F). Thus, we also performed TEM of *U-E* leaf mesophyll cells to identify any effect of ectopic overexpression of *Zmufo1*. Around 25% of *U-E* mesophyll cells showed up to 3 large EDRs compared with 7 to 10 EDRs in all WT, and *U-S* nuclei (Fig. 6G). As *Zmufo1* expression is endosperm-specific but *Ufo1-1* is ectopically expressed in *U-E*, we performed TEM on the *U-E* leaf tissue but not on *ufo1-Dsg*.

We further used *Zmp1*, the classical epigenetic target of *Ufo1-1* as a reporter to detect histone modifications (Fig. 7). *Zmp1* is manyfold overexpressed in *U-E* causing high flavonoid pigmentation in the pericarp, husk, silk, and tassel as well as in leaf sheath (Wittmeyer et al. 2018). The *Zmp1* promoter and gene body regions are enriched in fragments of retrotransposons and DNA transposable elements that are known hallmarks of DNA methylation and chromatin modification-mediated gene silencing (Lisch 2009; Hirsch and Springer 2017). The *Zmp1* distal enhancer (DE/P1.2) contains a MULE (mutator-like element) and is a target of DNA methylation modifications in the presence of *U-E* (Chopra et al. 2003; Sekhon and Chopra 2009). We detected a reduction of the H3K9me2 and H3K27me3 enrichment in DE as well as gene body regions. We also found a reduction of these chromatin methylation marks at the proximal enhancer (PE), which contains partial fragments of a Tourist (Pr-3), a MULE (Pr-2), and a captured intron (Pr-1) of a *Calcium-dependent protein kinase39* (Fig. 7). These results may further indicate the role of *Zmufo1* in maintaining chromatin structure, especially for repetitive and transposon sequences.

ZmUFO1 is localized in nucleus, nucleolus, and interacts with chromatin remodelers

To further understand the molecular function of the ZmUFO1 protein, we performed subcellular localization using green fluorescent

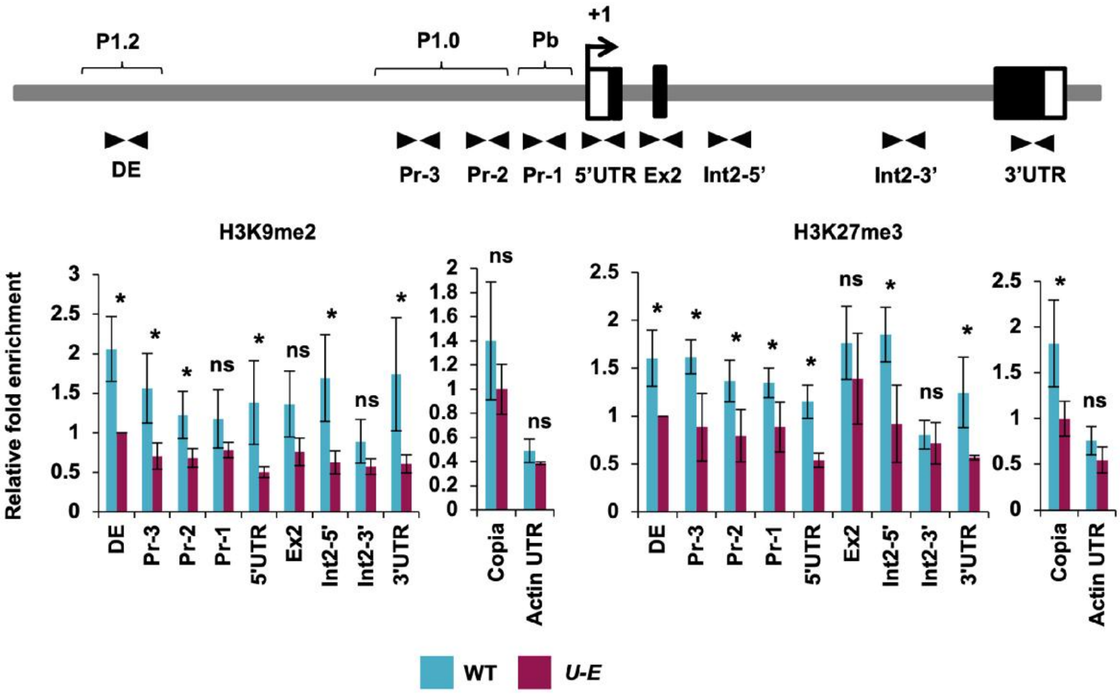

Figure 7. Enrichment of histone methylation marks on *pericarp color1* (*Zmp1*) in *U-E* plants. Schematic diagram showing *Zmp1* promoter, gene body regions, and RT-qPCR primers designed for specific regions (DE, distal enhancer; Pr-3, primer-3; Pr-2, primer-2; Pr-1, primer-1 regions of proximal enhancer comprising P1.0 and Pb; 5′UTR and 3′UTR, 5′ and 3′ untranslated regions, respectively; EX2, exon2; Int2-5′ and Int2-3′ primers of intron2) of *Zmp1*. Chromatin immunoprecipitation (ChIP) followed by RT-qPCR (ChIP-RT-qPCR) assay for enrichment of H3K9me2 and H3K27me3 on *Zmp1* from 18 days after pollination pericarps. The relative fold change is calculated using the ChIP efficiency of *P1-wr/P1-wr*; +/+ as control. Results shown are mean ± SE. A total of 30 independent kernels comprising 10 kernels from 3 independent ears were used. Asterisk (*) indicates significance at $P \leq 0.05$ using Student's *t*-test.

protein (GFP) fusion (Fig. 8). Transiently expressed C terminus UFO1-GFP fusion protein under the control of cauliflower mosaic virus 35S promoter (CaMV35S) showed fluorescence signal enrichment in the nucleolar rim and diffused signal in the nucleoplasm of *Nicotiana benthamiana* leaf epidermal cells (Fig. 8A). The negative control showed a low-intensity diffused GFP signal throughout the cytoplasm (Fig. 8A). The 4′,6-diamidino-2-phenylindole dihydrochloride (DAPI) staining of the nucleus and dark cavity of nucleolus overlapped with UFO1-GFP fluorescence confirming its nuclear and nucleolar localization (Fig. 8B). We further co-localized UFO1-GFP with a nucleolar marker *fibrillarin1* tagged with a yellow fluorescent protein (YFP) under the control of CaMV 35S promoter (FIB1-YFP) for additional confirmation (Barneche et al. 2000; Pontvianne et al. 2013; Fig. 8C).

Next, we performed a Yeast two-hybrid (Y2H) screen using a 10 DAP kernel cDNA library to detect the interacting protein partners of ZmUFO1. Full-length ZmUFO1$^{1–326AA}$ bait resulted in toxicity and a high background, likely due to the presence of an activation domain (AD). Therefore, 2 truncated baits, ZmUFO1$^{1-130AA}$ and ZmUFO1$^{110-326AA}$, were used (Supplementary Fig. S5). Due to the self-activation of ZmUFO1$^{110-326AA}$, only the ZmUFO1$^{1-130AA}$ bait was selected for further Y2H screening (ULTImate Y2H, Hybrigenics Services, Paris, France) (Supplementary Fig. S6). From the screening of 111 million clones/yeast (*Saccharomyces cerevisiae*) transformants (11× library complexity), we identified 26 high-confidence proteins that interacted with ZmUFO1$^{1-130AA}$ (Supplementary Table S2). Y2H identified 14 of 26 ZmUFO1-interacting proteins have either redox-sensitive cysteine (C) motif CxxC (where x is any or preferably hydrophobic amino acid residue) or CxxC derived CxxS, CxxT, TxxC motifs (S-serine; T-threonine) that causes formation, isomerization, and reduction of disulfide bonds for other redox responsive functions (Supplementary Table S2; Fomenko and Gladyshev 2003; Fomenko et al. 2007; Matuleviciute et al. 2021). Y2H screen also identified a succinate dehydrogenase (ZmSUDH8A) and a peroxisomal membrane carrier protein associated with the maintenance of cellular redox state (Supplementary Table S2). The peroxisomal membrane carrier proteins are involved in peroxisomal β-oxidation crucial to maintaining acidification in cereal endosperm required for α-amylase activities (Drozdowicz and Jones 1995; Linka and Esser 2012).

Four of 26 proteins were phylogenetically related methyl-CpG-binding domain (MBD) proteins; ZmMBD101, ZmMBD111, ZmMBD108, and ZmMBD115 involved in the maintenance of repressive chromatin (Snape 2000; Questa et al. 2016). Four other proteins histone acetyltransferase1 (ZmHAC1), enhancer of polycomb-like protein (ZmEPL1), Condensin-2 complex subunit H2, and a methyltransferase-related protein (ZmMETTL1) are associated with transcriptional regulation through histone remodeling (Fina et al. 2017). Another 4 proteins, abscisic acid stress ripening5 (ZmAASR5), C2C2-GATA-transcription factor 8 (ZmGATA8), octopine synthase binding factor1 (ZmOBF1), and LIM-transcription factor13 (ZmLIMTF13) are TFs. Interestingly, light-responsive ZmGATA8 and a ZmAASR5-related protein ZmAASR1 are involved in long-range chromatin interaction (Walley et al. 2016; Li et al. 2019; Zhang et al. 2019b). Moreover, 3 proteins, nuclear pore complex NUP88 isoform1 (ZmNUP88), Importin 3 (ZmIMP3), and auxin transporter-like1 (ZmATL1) are associated with protein import and export from the nucleus. Other proteins were cyclophilin-type peptidyl-prolyl *cis-trans* isomerase (ZmCYP95), an SAP (SAF-A/B, Acinus, and PIAS) domain-containing protein (ZmSAP1), small

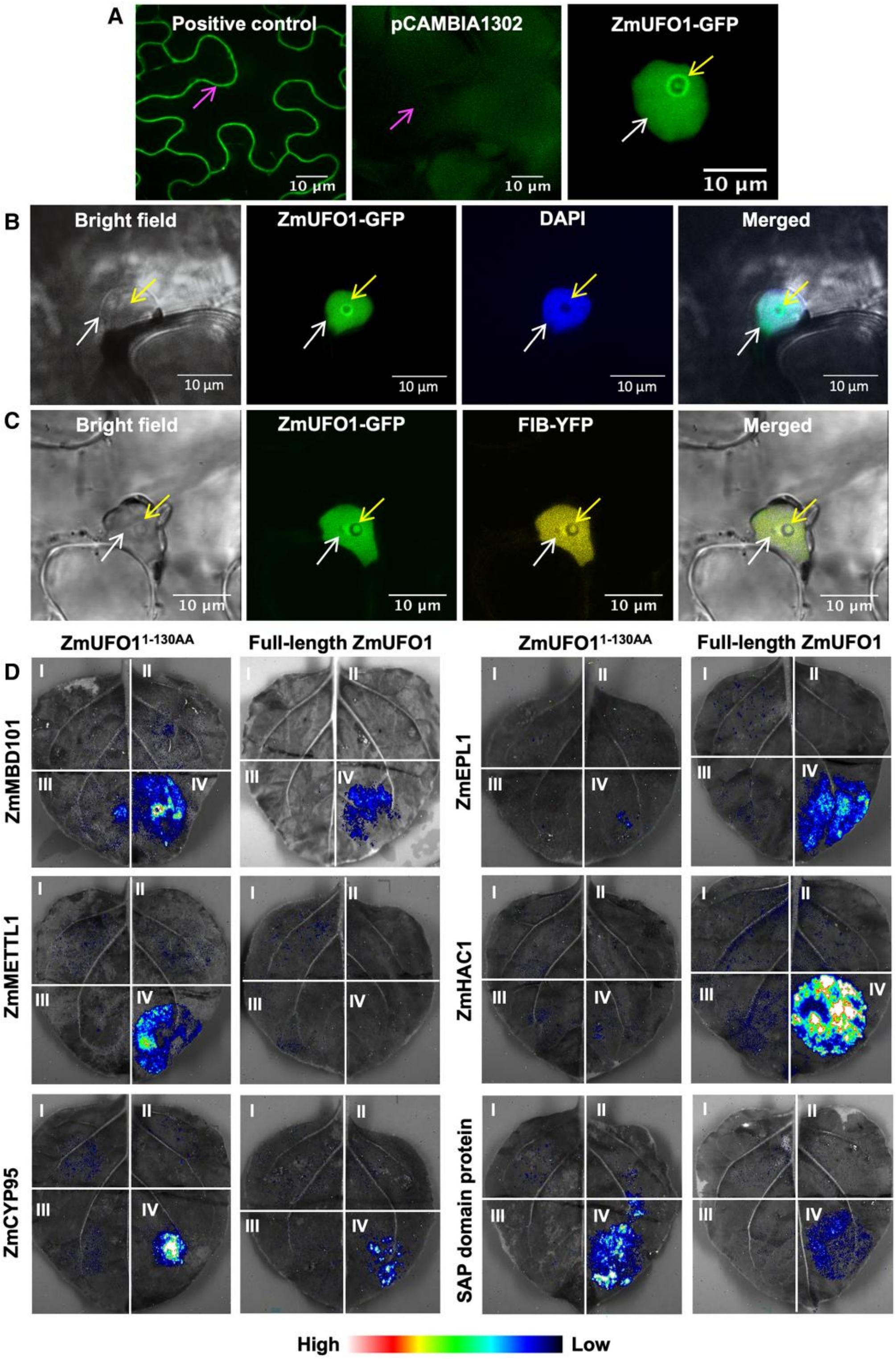

Figure 8. The *Zmufo1* protein (ZmUFO1) localizes to the nucleus and nucleolus and interacts with different nuclear proteins. **A)** Subcellular localization of transiently expressed cell membrane and plasmodesmata localizing wild-type movement protein, GFP:MPwt used as a positive control for experimental conditions, pCAMBIA1302 as the negative control, and C-terminal GFP fusion of the ZmUFO1 in pCAMBIA1302 (ZmUFO1-GFP) in nuclei and nucleoli of *Nicotiana benthamiana* leaf epidermal cells. **B)** Subcellular localization of transiently expressed ZmUFO1-GFP in nuclei and nucleoli. DAPI (6-diamidino-2-phenylindole, dihydrochloride) marked nuclei. **C)** Transient co-expression of ZmUFO1-GFP with YFP tagged fibrillarin (FIB-YFP). Magenta, white, and yellow arrows indicate cell membrane, nucleus, and nucleolus, of an epidermal cell, respectively, in **A** to **C)**. **D)** The luciferase complementation imaging (LCI) assay in *N. benthamiana* leaves showed the interactions of full-length ZmUFO1 and 1-130 amino acids of ZmUFO (ZmUFO1$^{1\text{-}130AA}$) with ZmMBD101 (*Zm00001d010322*), ZmEPL1 (*Zm00001d024088*), putative methyltransferase (*Zm00001d023366*), ZmHAC1 (*Zm00001d015209*), ZmCYP95 (*Zm00001d015729*), and a putative SAP domain protein (*Zm00001d006684*). The numbers I, II, III, and IV in each subpanel indicate empty N- and C-terminal luciferase (NLUC + CLUC), NLUC with bait, and empty CLUC, empty NLUC, and CLUC with the target protein, NLUC with bait and CLUC with the target protein, respectively. The scale indicates the gradient of luciferase signal intensity; white and red, a strong signal and blue and black, a weak signal.

subunit processome component 20 homolog (ZmUTP20), E3 ubiquitin-protein ligase 10 (ZmUPL10), and 60S ribosomal protein L19-2 (Supplementary Table S2). Yeast UTP20 is involved in 18S pre-rRNA processing and is associated with U3 small nucleolar RNA (Wang et al. 2007). Five randomly selected proteins among the 26 proteins, ZmMBD101, ZmMBD111, ZmIMP3, ZmSAP1, and ZmMETTL1 were further confirmed as interacting partners of ZmUFO1$^{1\text{-}130}$ using a 1-by-1 Y2H assay (Hybrigenics Services, Paris, France).

Next, we performed in vivo confirmation of 6 selected Y2H-identified proteins with luciferase complementation imaging (LCI) using both truncated ZmUFO1$^{1\text{–}130AA}$ and the full-length ZmUFO1$^{1\text{–}326AA}$ as baits (Fig. 8D; Supplementary Table S3). ZmUFO1$^{1\text{-}130AA}$ and full-length ZmUFO1$^{1\text{–}326AA}$ interacted with ZmMBD101, ZmCYP95, and ZmSAP1. ZmEPL1 and ZmHAC1 showed high luciferase signals only when interacting with full-length ZmUFO1$^{1\text{–}326AA}$. LCI assays being more precise than Y2H, this result indicates that the domain required for the interaction with ZmEPL1 and ZmHAC1 are potentially present within ~130 to 326 AA region of ZmUFO1. However, only ZmUFO1$^{1\text{-}130AA}$ which was used as a bait in the Y2H assay showed a high luciferase signal with ZmMETTL1.

Together, the results established that *Zmufo1* encodes a nuclear and nucleolar protein that interacts with diverse protein partners involved in redox state regulation, and nuclear functions such as epigenetic modification of chromatin, transcriptional regulation, nuclear transport, and unfolded protein response.

The disordered nature of ZmUFO1 protein

The deduced sequence of ZmUFO1 harbors predicted N-acetyltransferase, SANT (Swi3, Ada2, N-Cor, and TFIIIB), and H3-H4 histone chaperone anti-silencing function1 (ASF1) domain (Supplementary Fig. S7). The sorghum (Sobic.007G066566 and Sobic.007G066200), Setaria (LOC101754388), and rice (LOC_Os08g08880 and LOC_Os08g08900) orthologs of ZmUFO1 also harbor the ASF1 domain that shares similarity with that of ZmASF1, AtASF1A, and AtASF1b proteins (Supplementary Fig. S7A). Although the exact nature and function of ZmUFO1 is still enigmatic, its sequence has a predicted "IDR" at aa ~50 to 250 (disorder scores > 0.5 by PONDR web interface) (Molecular Kinetics, Indianapolis, USA) (Fig. 9A). Protein sequences of ZmUFO1 and its orthologs are rich in charged, polar, and proline amino acids, with only 20 to 24% hydrophobic residues compared with 30% present in average globular proteins (Barik et al. 2020). We cloned *Zmufo1* full-length cDNA in pET-30a(+) vector with hexa (6X) His-tag and expressed it in *E. Coli* (BL21 DE3) cells. While purifying recombinantly expressed ZmUFO1-His, we observed high turbidity of sample solutions at 4 °C which became clear upon raising the temperature to 25 °C. Differential interference contrast (DIC) microscopy observation of the solution of ZmUFO1-His at 4 °C revealed droplets or condensates, showing the coexistence of a dense and a dilute phase in the solution, indicating liquid–liquid phase separation (LLPS) (Fig. 9B). No condensate was observed in control protein bovine serum albumin (BSA) at 4 °C. At 25 °C, neither BSA nor ZmUFO1-His showed condensate formation. Further, dynamic light scattering (DLS) showed that at approximately 21.5 °C, a notable transition in size occurs (Fig. 9C). We observed large clusters up to 500 nm in size (average ~60 nm) forming LLPS within the temperature range of 4 to 21.5 °C (Supplementary Fig. S8). However, as the temperature increases beyond this threshold, there is a discernible shift towards the formation of smaller oligomeric clusters 4 to 60 nm in size (average ~20 nm) (Supplementary Fig. S8). Another notable structural event is observed with the onset of melting of the 3D structure occurring at approximately 60 °C that disrupts inter and intramolecular bonds critical for structural integrity (Fig. 9, D and E) forming aggregates greater than 1000 nm. This temperature marks a critical point at which the stability of the molecular structure begins to diminish.

The analysis of circular dichroism (CD) data provides insights into the secondary structure composition within the LLPS. Interestingly, the results indicate a predominant presence of β-sheets, constituting approximately 38% of the secondary structure (Fig. 9F). In contrast, helices are relatively less abundant, comprising only around 5% of the secondary structure. This distribution suggests a unique conformational arrangement characteristic of the LLPS state, with β-sheets playing a prominent role in the organization of the molecular assembly.

Discussion

The spontaneous *Ufo1-1* mutation was identified through overexpression of *Zmp1* and later shown to be an epigenetic modifier of *Zmp1*. *Zmp1* encodes an R2R3-MYB-like TF that regulates flavonoid biosynthesis and has also been predicted to target over 1,000 maize genes (Morohashi et al. 2012). Our results from plants carrying a nonfunctional *Zmp1* allele in *p1-ww;Ufo1-1* confirm that overexpression of *ZmUfo1-1* alone could cause some growth and developmental defects (Fig. 1). However, some overlaps among GO terms/processes identified in *U-E* and *P1-rr* pericarp transcriptomes are interesting and will be investigated in future studies (Supplementary Table S1). Interestingly, *Zmufo1* is downregulated in the mutant of an R2R3-MYB maize TF *dosage-effect defective1* (*ded1-ref*) that also showed incomplete endosperm development (Dai et al. 2022). However, *Zmufo1* was not detected as a direct target of *ded1*.

The maize genome eFP kernel browser (Doll et al. 2020) along with our previous characterization establishes the endosperm-specific expression of *Zmufo1* (Chatterjee et al. 2021). Moreover, *Zmufo1* has been identified as one of the critical hub genes for maize endosperm development (Xiong et al. 2017). In addition, *Zmufo1* has been shown to be co-expressed with genes crucial for endosperm development such as C2C2-Dof-transcription factor 36 (*Zmdof36*) and MYB-transcription factor155 (*Zmmyb155*) (Zhou et al. 2020). We demonstrated here that mutations in *Zmufo1* cause transfer cell defects in basal endosperm. However, the defects are not always identical among *ufo1-Dsg* and *U-E*. For example, the BETCs in *ufo1-Dsg* are small and deformed, whereas BETCs in *U-E* are not fully defective but have shorter CWIs. Although *ENB1* that encodes a cellulose synthase 5 implicated in the synthesis of CWIs (Wang et al. 2021) was not a DEG in our transcriptomes, we found that several BETC-specific genes have altered expression in both *U-E* and *ufo1-Dsg* (Fig. 2D; Supplementary Fig. S4). This was further supported by GUS expression in BETC of *proBETL1::GUS* transgenic plants that morphology between these 2 mutants could be associated with the upregulation of BETC genes in *U-E* but their downregulation in *ufo1-Dsg* (Fig. 2, E and F). As shown previously, the *U-E* plants produce excess sugar in leaves but experience blockage of sugar transport in SE due to the abnormal development of BETCs (Wittmeyer et al. 2018; Chatterjee et al. 2021). Excessive accumulation of hexoses in PC as early as 8 DAP can influence the expression of the BETC marker genes (Doll et al. 2017) in *U-E*, as many of them are hexose-sensitive. Similar contrasting observation was made among the gene expression of *Zmrad51a*, *Zmku70*, and *Zmku80* where all 3 genes had high expression in *U-E* but no notable expression change in *ufo1-Dsg* (Fig. 3F). Although these genes are commonly associated with DDR, they have multifaceted functions

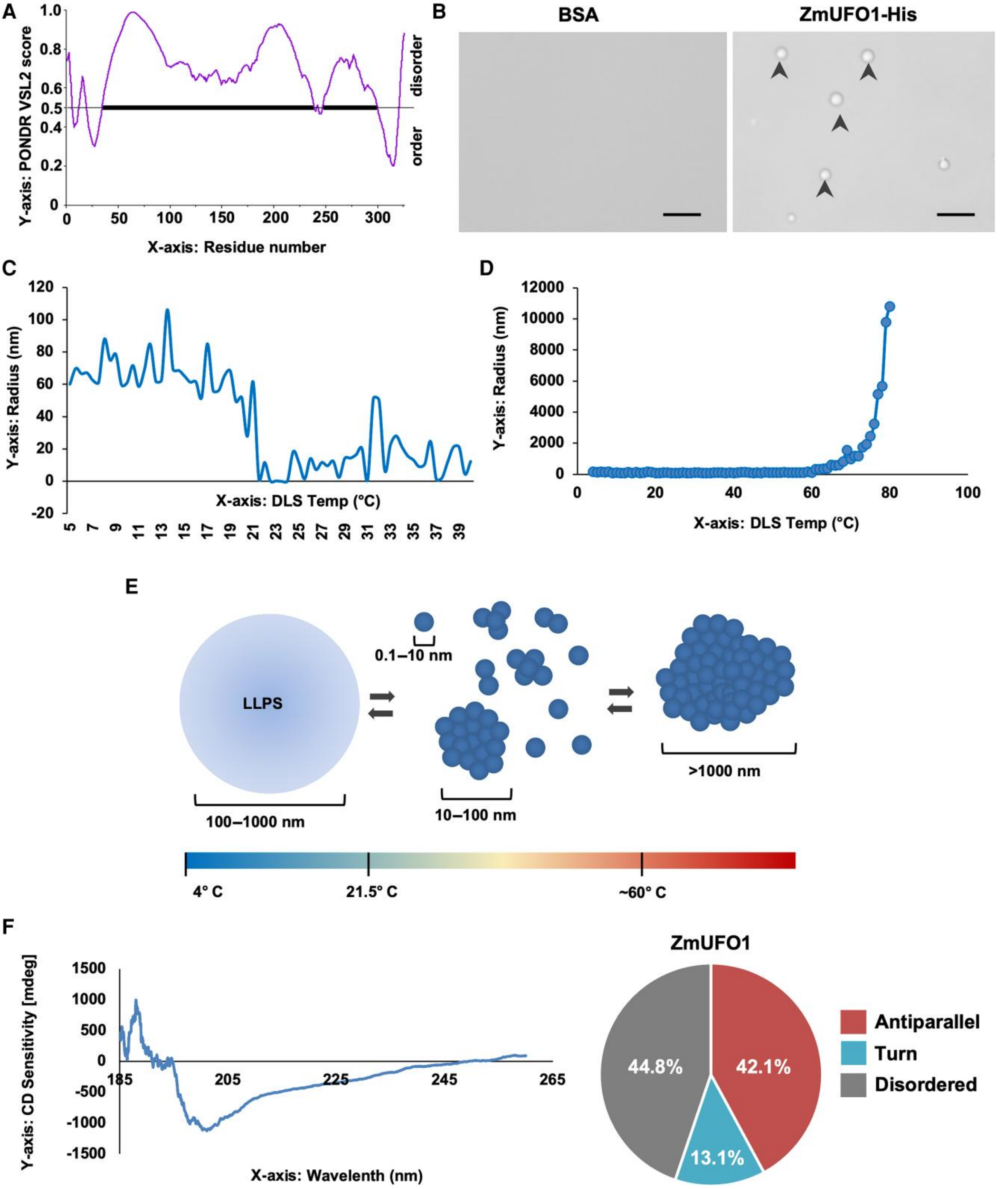

Figure 9. The disordered nature of ZmUFO1. **A)** Intrinsically disordered regions (IDRs) prediction in ZmUFO1 deduced sequence using PONDR web interface. The default threshold value (0.5) is indicated by a black horizontal line above which a protein region is considered as disordered. The thick black horizontal line shows IDRs defined as regions with PONDR scores equal to or higher than 0.5 for at least 50 amino acids. **B)** Representative differential interference contrast microscopy images showing the droplets formed by ZmUFO1-His proteins as compared with no droplet formation in negative control bovine serum albumin (BSA) at 4 °C. Scale bar = 20 μm. Black arrowheads indicate droplets. **C)** Dynamic light scattering (DLS) measurements showing the changes in ZmUFO1 mean hydrodynamic radius with change in temperature of the protein solution. **D)** DLS results show a dramatic change in the average hydrodynamic radius with temperature change above 60 °C. **E)** An illustration of the transition from liquid–liquid phase separation (LLPS) to a mixture of oligomers and monomers of ZmUFO1 above 21 °C and aggregates above 60 °C. **F)** Circular dichroism spectroscopy (CD) showing a low helix but a high antiparallel percentage in 0.8 mg ml^{-1} ZmUFO1-His in phosphate-buffered saline. The CD data is obtained as ellipticity (θ), which is related to absorbance by a factor of 32.98 ($\theta = 32.98\ \Delta\text{Abs}$) and is represented as millidegrees (mdeg). The pie diagram shows the different secondary structures in the multimeric form of ZmUFO1.

including cell cycle, transcription, translation, and ribosome biogenesis, and can be influenced by redox changes (Andrews et al. 2006; Kelly et al. 2023). Due to the pleiotropic nature of the overexpression of *Ufo1-1*, multiple biological processes are affected in *U-E* which could have a cumulative effect on the expression of these marker genes resulting in unpredictable expression patterns.

Despite, the expression differences of marker genes and the types of BETL developmental defects, we found similarities in abnormal ROS accumulation, oxidative DNA damage, and cell death patterns between *ufo1-Dsg* and *U-E*. Thus, we hypothesize that mere deviation in the expression pattern of some crucial genes, whether they are up- or downregulated, might affect the homeostasis of ROS and DNA damage in both *ufo1-Dsg* and *U-E*. Moreover, despite high ROS accumulation, the spatial distribution of excess ROS is not identical between *U-E* and *ufo1-Dsg*. At 10 and 16 DAP, complete *U-E* endosperm showed high NBT staining (for superoxide) whereas *ufo1-Dsg* had intense NBT staining only in the basal endosperm region (Fig. 3A). High ROS and oxidative DNA damage in *U-E* could be influenced by high sugar accumulation. In fact, DNA damage at guanosine residues, can also result from glycation when the sugar level is high (Tripathi et al. 2023). One of the sources of increased ROS in *ufo1-Dsg* could be differential expression of the TCAC genes succinate dehydrogenase, isocitrate dehydrogenase, 2-oxoglutarate dehydrogenase E1 (Fig. 5) whose misregulation has been shown to cause high ROS accumulation (Berg and de Kok 1997; Tretter and Adam-Vizi 2005; Brown et al. 2008; Jardim-Messeder et al. 2015; Condori-Apfata et al. 2019). Differential expression of mitochondrial pentatricopeptide repeat (PPR) protein-encoding genes in *ufo1-Dsg* kernel may also cause excessive ROS and mitochondrial dysfunction leading to BETC defects as observed in maize mutants *dek40*, *dek35*, *dek504*, *emp4*, and *ppr78* (Taylor et al. 2004; Gutiérrez-Marcos et al. 2007; Chen et al. 2017b; Zhang et al. 2017; Ren et al. 2019; Fan et al. 2021; Ma et al. 2022; Wang et al. 2022). Irrespective of the cause of abnormal ROS accumulation, just the change in ROS gradient could affect the BETL development in *ufo1-Dsg* and *U-E* similar to what was observed in *sks13* and *smk10* maize mutants and in faba beans (Zhou et al. 2010; Offler and Patrick 2020; Xia et al. 2020; Hu et al. 2021; Zhang et al. 2021). The antioxidant supplementation assay (Fig. 4) confirms that just reverting abnormal ROS to near-normal levels could almost restore the BETC developmental defects of *ufo1-Dsg* and *U-E*.

Remarkably high levels of acetyl-CoA detected in basal endosperms of *U-E* and *ufo1-Dsg* could be associated with abnormal expression of TCAC genes, high sugar, ROS, as well as perturbed histone modifications (Du et al. 2013; Chen et al. 2017a; Meng et al. 2020). However, further study is required to establish a direct cause–effect relationship among misregulation of *Zmufo1*, abnormal accumulation of ROS and acetyl-CoA. Sparse EDRs in the nuclei of CZ cells in both *U-E* and *ufo1-Dsg* indicated abnormal heterochromatin and attenuation of transcriptional repression (Fig. 6E), which is further supported by reduced H3K9me2 and H3K27me3 marks at the *Zmp1* that is overexpressed in *U-E* (Fig. 7). Several DEGs in *ufo1-Dsg* and *U-E* are associated with the PRC2 which is induced by ROS and regulates H3K27me3-mediated silencing (Supplementary Fig. S4; Boros et al. 2014; Wiles and Selker 2017; Lavarone et al. 2019; Guo et al. 2021; Baile et al. 2022; Ye et al. 2022). Moreover, *U-E* pericarp and *ufo1-Dsg* kernel transcriptome show abnormal expression of various TFs and chromatin remodelers as observed in mutants defective for polycomb, mediator, Piccolo NuA4, and elongator complexes (Fig. 5; Supplementary Fig. S4; Galarneau et al. 2000; Dolan et al. 2017; Jarosz et al. 2020; Chen et al. 2022). In fact, the Arabidopsis ortholog of ZmEPL1, an interacting partner of ZmUFO1, is a component of the Piccolo NuA4 complex that acetylates EPL1 to promote heterochromatin silencing, transcription, and cell proliferation, and to prevent spurious activation of stress response genes (Galarneau et al. 2000; Latrasse et al. 2008; Chittuluru et al. 2011; Mitchell et al. 2013; Searle et al. 2017; Crevillén et al. 2019; Espinosa-Cores et al. 2020; Bieluszewski et al. 2022).

The Y2H and LCI assays revealed that ZmUFO1 interacts with a diverse group of proteins involved in chromatin remodeling, long-range chromatin interaction, transcriptional regulation, nuclear transport, ribosomal functions, and redox state regulation (Supplementary Fig. S7A). Interestingly, 17 and 13 of the 26 Y2H-identified proteins have 1 or more nuclear (NLS) and nucleolar localizing sequence (NoLS), respectively. NLSs are predominantly short sequence motifs of nuclear import machinery targeting the nuclear membrane, whereas NoLSs have a high affinity to nucleolar core components such as ribosomal DNA, RNA, or nucleolar proteins (Carmo-Fonseca et al. 2000; Scott et al. 2010, 2011). Although we could not detect NLS or NoLS in ZmMETTL1, ZmHAC1, ZmAASR5, ZmCHC1, ZmSUDH8A, and ZmATL1, their potential role in the nucleus or nucleolus cannot be ruled out without further studies. ZmUFO1-interacting TCAC protein ZmSUDH8A may have a role in transcriptional activation, and histone modification besides ROS regulation (Cervera et al. 2009). The hypothesized role of ZmUFO1 in chromatin remodeling is further supported by the predicted ASF1 domain of ZmUFO1 which is known to be crucial for nucleosome assembly and DDR (Zhu et al. 2011; Maulión et al. 2019; Casati and Gomez 2021; Supplementary Fig. S7, B and C; Supplementary Text S1). ZmHAC1, an interacting partner of ZmUFO1, has a predicted Rtt109 HAT domain known to be activated by the ASF1 (Supplementary Fig. S7D; D'Arcy and Luger 2011). ZmHAC1 also has a TAZ-type zinc finger domain that binds to intrinsically disordered regions (IDRs) (De GuZman et al. 2005; D'Arcy and Luger 2011; Dyson and Wright 2016). HACs were reported to interact with MBDs, importins, and chromatin-associated NUPs (Fujita et al. 2003; Ryan et al. 2006). We speculate that ZmHAC1 could have a 2-fold function, first in activating the ZmUFO1 and, second, in providing a flexible, IDR domain that could interact with additional diverse proteins. ZmUFO1 is localized in the nucleolar rim which is known to be enriched in intrinsically disordered proteins (IDPs) tethering the nucleolus to the chromatin (Stenström et al. 2020). The predicted IDR in ZmUFO1 (Fig. 9A) may facilitate its interaction with multiple and diverse proteins as observed in the Y2H assay.

The DIC microscopy, CD, and DLS results provide a comprehensive understanding of structural dynamics, temperature-dependent transitions, and the organization of molecular assemblies of ZmUFO1 in vitro (Fig. 9). The DLS results show a transition from large clusters to smaller oligomeric clusters at 21.5 °C, indicating altered molecular organization likely due to temperature-induced structural changes and alterations in intermolecular interactions (Fig. 9, C to E). Within large clusters at 25 °C, 38% of β-sheets suggest a conformation favoring extended β-sheets over helices. Prediction programs further identify highly disordered segments aligned with our finding of >50% flexible regions underscoring the assembly's dynamic nature crucial for accommodating unique structural transitions and interactions (Fig. 9E). Together these results further support the hypothesis that the ZmUFO1 IDR is involved in the oligomer formation required for multifaceted interaction with diverse proteins (Huang et al. 2021). The deduced sequence of ZmUFO1 shows the presence of redox-sensitive disordered residues in the IUPred2A prediction web interface (Mészáros et al. 2018). Cellular redox induces accumulation of IDPs in a biomolecular condensate causing LLPS and sequestration of developmentally regulated promoters

(Huang et al. 2021). Our findings, so far, indicate that ZmUFO1 may be associated with a redox-sensitive protein complex that attenuates repression of chromatin during the early stages of endosperm development. Further study of the disordered nature of ZmUFO1 and its interaction with chromatin, ROS, and its protein partners *in-planta* may elucidate a mechanism of spatiotemporal transcriptional regulation in basal endosperm.

Materials and methods

Plant materials

All plants were grown at the Russell E. Larson Agricultural Research Center, the Pennsylvania State University, Rock Springs, Pennsylvania, USA. Unless otherwise indicated, all inbreds and genetic stocks were obtained from the Maize Genetics Cooperation Stock Center, USDA-ARS. The original *ZmUfo1-1* maize (*Z. mays* L.) mutant stock was received from Dr. Derek Styles and introgressed into B73 inbred (Chopra et al. 2003; Wittmeyer et al. 2018; Chatterjee et al. 2021). The *U-E* and *U-S* NILs were developed from crosses between the original *Ufo1-1* stock as explained previously (Supplementary Materials and Methods S1; Wittmeyer et al. 2018; Chatterjee et al. 2021).

The seeds of loss-of-function *tdsgR80A05* allele (*ufo1-Dsg*) were identified from Dr. Hugo K. Dooner's *Ac/Ds* new reverse genetics resources (http://www.acdsinsertions.org/) and obtained from maize genetics cooperation stock center, USDA-ARS, Illinois, genotyped to isolate homozygous progeny plants, and characterized as described previously (Chatterjee et al. 2021).

The selfed *proBETL1::GUS* transgenic seeds of hemizygous line PB-T-12: 240-3 (BETL1-GUS/-) were obtained from Dr. Phillip Becraft, Iowa State University, IA, USA. Homozygous *proBETL1::GUS* plants were isolated by genotyping (primers are listed in Supplementary Table S4; Supplementary Materials and Methods S2). Seeds from the transgene negative segregants were used as a negative control for GUS staining. F_1 seeds from crosses between *proBETL1::GUS* and *U-E* or *ufo1-Dsg* were used for GUS assay with *proBETL::GUS* as a positive control.

Light microscopy

For light microscopy, 10 kernels of 10 DAP from 3 independent ears per genotype were dissected along the longitudinal axis and immediately fixed in a formalin–acetic acid–ethanol mixture followed by dehydration in an ethanol gradient of (50%, 60%, 70%, 85%, 95%, and 100%) v/v in a TP1020 paraffin processor (Leica, Wetzlar, Germany). Paraffin-infiltrated sections were dissected while mounted on positively charged slides using the Thermo Scientific Shandon Finesse ME Microtome (Cambridge, UK) and deparaffined using an Autostainer ST5010 XL (Leica, Wetzlar, Germany). Deparaffined sections were manually stained with toluidine blue O. Twenty sections from 20 individual kernels per genotype were observed and representative images were taken using a BZ-9000 E Microscope (Keyence, Osaka, Japan).

Scanning electron microscopy

Kernels at 10 DAP from 3 independent ears per genotype were dissected along the longitudinal axis and immediately fixed in FAA (Formaldehyde alcohol acetic acid, 10%:50%:5%+35% water) solution until further use. An EM CPD300 Critical Point Dryer (Leica, Wetzlar, Germany) was used for critical drying. Samples were coated with gold particles using Bal-tec SCD-050 Sputter Coater (Bal-tec AG, Balzers, Liechtenstein). A SIGMA VP-FESEM (SEM) (Zeiss, Oberkochen, Germany) was used for imaging.

RNA extraction, first-strand cDNA synthesis, and RT-qPCR

Twenty 10 DAP kernels were sampled per genotype from independent ears from the individual plant for whole kernel assay. For the basal endosperm assays, 30 kernels from independent ears were sampled per genotype and dissected to remove the pericarp and upper two-thirds of the endosperm. Total RNA was extracted using RNAzol (Molecular Research Center, Cincinnati, OH) following the manufacturer's instructions and was reverse transcribed to the first-strand cDNA with oligo-dT primers using the high-capacity cDNA reverse transcription kit (Applied Biosystems, Foster City, CA, USA). RT-qPCR assays were performed using 10 ng first-strand cDNA and FastStart universal SYBR green RT-PCR master mix kit (Roche Applied Science, Penzberg, Germany). All PCRs were performed as described previously (Wittmeyer et al. 2018). The average from 3 independent assays was used as the final value for each sample. The primers used are listed in Supplementary Table S5.

β-glucuronidase (GUS) assay

Tissues were stained for GUS activity in a solution containing 0.5 mg ml^{-1} X-glucuronide, 0.5 mM potassium ferrocyanide, 0.5 mM potassium ferricyanide, 10 mM Na_2EDTA, 50 mM phosphate buffer, pH 7, 0.1% Triton X-100, and 20% (v/v) methanol and counterstained with Safranin O (Sigma-Aldrich, St. Louis, MI, USA) in 50% EtOH (Jefferson et al. 1987). Kernels of nontransgenic segregants without the *proBETL1::GUS* were used as negative controls. Ten kernels per 3 independent ears per genotype were used for the experiment and the images were taken using an SMZ1000 stereo microscope and DXM1200F Microscope CCD Camera (Nikon, Minato City, Tokyo, Japan).

Leaf epidermal impressions and propidium iodide staining

For stomata defects, glue impression of epidermis were collected from abaxial surfaces of fully opened V3 leaves. Twenty independent impressions or epidermal sections were collected from 3 independent plants per genotypes. Samples were stained with propidium iodide and visualized using an Eclipse 80i microscope attached with RFP filter (excitation, 540 to 580 nm; band-pass barrier filter, 600 nm; emission, 635 nm), DXM1200F Microscope CCD Camera (Nikon, Minato City, Tokyo, Japan) and Mercury-100 W Lamp Power Supply (Optical Apparatus Co., Ardmore, PA, USA) using 200-ms exposure and 300 gain.

Quantification of sucrose, glucose, fructose, and raffinose

Ten seeds from independent ears of 3 individual plants per genotype were used. Kernels from the antioxidant treatment assay after completion of the treatments (for sucrose, glucose, and fructose), 24 DAP kernels, and the whole mature dry seeds (MDS) (for raffinose) were homogenized for analysis. The youngest leaves from 4 individual V3 plants per genotype were sampled before the end of the photoperiod. Sugar extraction was performed based on the methods described (LeClere et al. 2010; Leach and Braun 2016). Quantification was done using commercial kits for Saccharose (Sucrose)/D-Glucose/D-Fructose (10716260035), and raffinose (10428191035) (R-Biopharm, Pfungstadt, Germany) following the manufacturer's instructions in 96-well flat-bottom polystyrene plates and using a Cytation3 imaging reader (BioTek, Winooski, VT, USA). The average values from 3 independent measurements were used as the final values for each sample.

Detection of hydrogen peroxide (H_2O_2) and superoxide anions

NBT and 3,3′-diaminobenzidine (DAB) were used for ROS staining. For NBT staining, the kernels were longitudinally cut in halves, incubated in dark at room temperature for 3 h in a 0.5 mg ml^{-1} NBT solution in 10 mM potassium phosphate buffer (pH 7.6). For DAB staining, the kernels were similarly cut in longitudinal halves, incubated in 1 mg ml^{-1} DAB in 50 mM Tris-HCl buffer (pH 5.0) in the dark for 16 h at 37 °C. The staining solution was decanted off and samples were decolorized with ethanol gradient. Thirty kernels per genotype for each timepoint were evaluated. The representative samples were photographed with an SMZ1000 stereo microscope and DXM1200F Microscope CCD Camera (Nikon, Minato City, Tokyo, Japan).

Quantification of hydrogen peroxide (H_2O_2)

Hydrogen peroxide content was evaluated spectrophotometrically after reaction with KI (Alexieva et al. 2001). In a pre-chilled mortar and pestle, 0.5 g of kernel tissues were ground in 0.1% trichloroacetic acid (TCA). The extracts were then centrifuged at 12,000 rpm for 15 min. The reaction mixture consisted of 0.5 ml 0.1% TCA kernel extract supernatant, 0.5 ml of 100 mm K-phosphate buffer, and 2 ml reagent (1 M KI w/v in fresh double-distilled water). The blank probe consisted of 0.1% TCA without kernel extract. The reaction was incubated at room temperature for 1 h in dark and absorbance was measured at 390 nm. The amount of hydrogen peroxide was calculated using a standard curve prepared with known concentrations of H_2O_2.

RNA-Seq analysis

Transcriptomes generated from the V10 and 18 DAP pericarp have been described previously (Wittmeyer et al. 2018). These transcriptomes were generated before cloning of *Zmufo1* based on the prominent phenotypes of the *U-E* plants. The 18 DAP pericarp was selected due to the dominant flavonoid accumulation phenotype. The *U-S* leaf tissue was selected due to WT-like phenotypes (Wittmeyer et al. 2018). For *ufo1-Dsg* and W22 10 DAP kernel transcriptomes, total RNA from 2 biological replications per genotype were used. Each biological replication comprised 20 seeds from each of the 3 independent plants. Raw reads were aligned and counted using STAR RNA-Seq aligner (Dobin et al. 2013) for each gene model and normalized the row counts with the edgeR (Robinson et al. 2010; McCarthy et al. 2012) R package. The Benjamini–Hochberg method (Haynes 2013) was followed to control the false discovery rate (FDR) and derive the adjusted *P*-value using edgeR for identifying DEGs between samples. GO term and Z-score were analyzed by PAGE analysis in (agriGO v2.0), which provided the GO terms, the number of genes in the GO terms, and the Z-score for each sample (Haynes 2013; Tian et al. 2017). Gene names and descriptions for heatmaps were downloaded from maizegdb.org, gramene.org, and phytozome.jgi.doe.gov. The heatmaps were created using the ggplot2 data visualization package in RStudio (https://rstudio.com/) (Villanueva and Chen 2019).

Terminal deoxynucleotidyl TUNEL

Fluorescence labeling of the sectioned kernels for TUNEL assays was performed with fluorescein in situ cell death detection kit (Roche, Basel, Switzerland) according to the manufacturer's instructions. The samples were photographed using an Eclipse 80i microscope attached to DXM1200F Microscope CCD Camera (Nikon, Minato City, Tokyo, Japan). Fifty individual microscopic FOVs were used to calculate the frequency of TUNEL-positive cells per FOV.

Evaluation of oxidative DNA damage

The oxidative DNA damage was detected in 5 DAG root tips and 10 DAP kernels. DNA was extracted from root tips and endosperms using a modified CTAB method (Supplementary Materials and Methods S2). The 8-OHdG detection and quantification in total DNA was performed using the EpiQuik 8-OHdG DNA Damage Quantification Direct Kit (EpiGentek, New York, USA) according to the manufacturer's instructions. The amount of 8-OHdG was calculated as the percentage of 8-OHdG of total DNA. For each genotype and tissue type, 3 independent replications were analyzed, and results from 3 independent technical replicates were combined to generate single data points.

Supplementation of developing kernels with exogenous antioxidants

In vitro kernel cultures were performed as described previously with minor modifications (Cheng and Chourey 1999; Sosso et al. 2015; Wang et al. 2021). Briefly, the ears from independent plants were harvested at 10 DAP, husks removed, and sterilized with 95% (v/v) ethanol and 5% (v/v) bleach for 5 min in a laminar flow. The cobs with attached kernels were dissected with a scalpel into blocks and placed in Petri plates with solid ½ MS media (M5519-5L; Sigma-Aldrich, St. Louis, MI, USA) (pH 5.8) with sucrose (1.5%, w/v), glucose (1.5%, w/v), 2,4-D (1 mg L^{-1}), cefotaxime sodium (300 mg L^{-1}), ascorbic acid (AsA, 1 mM), and glutathione (GSH, 1 mM) and cultured in a growth chamber at 28 °C in dark for 12 d. Kernels not treated with AsA and GSH were used as the mock-treated controls. Six biological replicates per genotype were used. Each biological replicate represents 9 individual kernels attached to glumes and a part of cob from an individual ear.

Quantification of acetyl-CoA

The acetyl-CoA content in the kernels of 10, 12, and 18 DAP kernels was determined with the PicoProbe Acetyl-CoA Fluorometric Assay Kit PicoProbe ab87546 (Abcam, Cambridge, UK). Three biological replicates per genotype were used for each time point. Each biological replicate represents basal endosperm dissected from 20 individual kernels from an individual ear.

HAT activity assay

The nuclei were isolated from basal endosperm dissected from 10, 12, and 18 DAP kernels using a nuclear extraction kit (00021) (EpiGentek, New York, USA). Three biological replicates per genotype were used for each time point. Each biological replicate represents basal endosperm dissected from 20 individual kernels from an individual ear. HAT activity was determined using the HAT Activity Colorimetric AssayKit (K332-100) (Abcam, Cambridge, UK). The nuclear extracts were assayed in a 96-well plate. For background reading, 10 ml of water was added into the sample instead of HAT substrates I and II; and for positive control, 10 ml of the cell nuclear extract and 30 ml of water was added. Assay mix was added to each well to start the reaction. Plates were incubated at 37 °C for 3 h for color development, and the absorbance was read on at 440 nm wavelength using Cytation3 imaging reader (BioTek, Winooski, VT, USA).

Transmission electron microscopy

The 15 DAP kernels were longitudinally cut into 2 halves with the embryo facing down and 1 mm^2 sections from the CZ-SE interface were visualized under an SMZ1000 Zoom stereomicroscope

(Nikon, Minato City, Tokyo, Japan). The mid-section of fully opened youngest leaves of V6 maize plants were cut into 1 mm^2 pieces and used. Three biological replicates per genotype were used. Each biological replicates represent 20 individual kernels from an ear or 20 1 mm^2 pieces from 1 leaf each of 3 independent plants. The sections were fixed in 4% glutaraldehyde, 1% paraformaldehyde, 0.3% Tween 20 (v/v), and 50-mM sodium cacodylate (pH 7.4) in a vacuum for 3 h before storing at 4 °C for further processing.

Samples were washed in 1 M cacodylate buffer (pH 7.4), postfixed in 1% OsO4/.1 M cacodylate overnight in the dark, followed by washing with DI H_2O, and staining with 1% uranyl acetate aqueous solution (60 min). After dehydration in an acetone gradient (50%, 70%, and 90% acetone, 30 min each step, 3 changes of 100% acetone, 30 min each), samples were transferred to acetone: Spurr solution and gradually embedded in acrylic resin using acetone: Spurr gradients (3:1 for overnight, followed by 1:1 for 8 h, 1:2, overnight, 100% Spurr, overnight on the rotator, 100% Spurr resin, 8 to 10 h in an open vial on a rotator and heated with a light bulb, 100% Spurr, overnight in an open vial on a rotator and heated with a light bulb). Next, samples were placed onto the flat mold with fresh 100% Spurr resin with desirable orientation and cured at 70 °C. Sections (70 nm) were made with a diamond knife Reichert Ultracut E microtome (Leica, Wetzlar, Germany). Sample sections were stained with uranyl acetate, poststained with lead citrate, and observed with a Hitachi H7600 transmission electron microscope (Hitachi High-Tech, Tokyo, Japan). At least, 20 individual microscopic fields were observed per tissue type for each genotype to confirm the results and representative images were taken.

Chromatin immunoprecipitation-quantitative real-time PCR

ChIP assays were performed using 18 DAP pericarps following a modified protocol as described previously (Haring et al. 2007; Kimura et al. 2008). Briefly, pericarps were cross-linked with 3% formaldehyde. The chromatin complex was then extracted and sheared to a size range of 0.5 to 1 kb fragments using a Bioruptor (Diagenode, Denville, NJ). The ChIP antibodies obtained from Dr. Hiroshi Kimura (Kimura et al. 2008) were then coupled with sheep anti-mouse IgG Dynabeads M-280 (Invitrogen, Grand Island, NY). Additionally, normal mouse IgG was used as a no antibody control (NoAb). The ChIPed DNA was further purified using QIAquick PCR Purification Kit (QIAGEN, Valencia, CA) and quantified via qPCR. ChIP-qPCR data was normalized using the percentage-of-input method. The relative differences between ChIP assay and input sample were determined using the ΔC_T method and presented as the relative fold enrichment. Data presented is a representative result of 3 independent experiments. The primers used are listed in Supplementary Table S6.

Subcellular localization

The coding sequence of *Zmufo1* cDNA was ligated into *NcoI* and *SpeI* restriction endonuclease sites of pCAMBIA1302 plasmid vector to develop pro35S:ZmUFO1-GFP construct (Primers listed in Supplementary Table S7). A plasmodesmata localizing pCG-GFP: MPwt (movement protein) under the control of CaMV 35S promoter was used as a positive control to standardize imaging conditions (Margaria et al. 2016). The resulting plasmids were transformed into *Agrobacterium tumefaciens* strain EH101. Agrobacterium cultures were mixed with P19 strain in a 1:1 ratio for enhanced expression. Cells were pelleted by centrifugation and resuspended in infiltration buffer (10 mM of MES at pH 5.7, 10 mM of $MgCl_2$, and 150 μM of acetosyringone) to a final cell density corresponding to OD_{600} of 1.0 before infiltration into the leaves of 5-wk-old *Nicotiana benthamiana* plants. *N. benthamiana* leaf abaxial epidermal cells were inoculated by Agrobacterium followed by incubation for 24 h at 25/21 °C day/night temperature in dark. The GFP fluorescence was visualized at 24, 36, and 48 h after inoculation. Leaf sections were stained with DAPI (1:100,000 of a 5 mg ml^{-1} stock; Sigma-Aldrich, St. Louis, MI, USA) prior to fluorescence visualization. Fifteen randomly chosen regions of interest from infiltrated leaves and ∼50 individual transformed cells were observed to confirm the result for each localization or co-localization experiment. Representative images were obtained using a Zeiss Axio Observer microscope with a Yokogawa CSU-X1 spinning disk head and a 20× or a 100× 1.4 NA oil immersion objective. A 405 nm excitation laser and a 450/50 nm emission filter were used for detecting DAPI, and a 488 nm excitation laser and a 525/50 nm emission filter were used for detecting GFP. A Zeiss LSM880 confocal microscope attached with a 34-channel NLO array detector was used to detect GFP and YFP using a 488 nm excitation laser and a 514 nm excitation laser, respectively, with 63× 1.4 NA oil immersion objective. Confocal images were collected with 90% laser power, 160-ms exposure, and 300 gain. Images were processed using Image-J software.

Y2H interaction assay

The full-length CDS of *Zmufo1* (981 bp) was amplified from the cDNA obtained from the total RNA of 10 DAP kernels of the B73 inbred line, using primers BD-UFO-F and BD-UFO-R (Supplementary Table S8). This fragment was then cloned into the pGBKT7 (BD) vector at the *EcoRI* and *BamHI* sites, using the MultiF Seamless Assembly Mix (ABclonal Technology, Hubei, China; cat. no. RM20523). The resulting construct, BD-ZmUFO1 (bait), was transformed into the yeast strain AH109. For the self-activation test, BD-ZmUFO1 and the empty pGADT7 (AD) vector were co-transformed into AH109, which showed that ZmUFO1 auto-activates the reporter system. Therefore, The ZmUFO1 corresponding cDNA was split into 2 fragments (amino acids 1 to 130 and 110 to 326) using primers BD-UFO-F/BD-UFO130AA-R and BD-UFO110AA-F/BD-UFO-R, respectively. These fragments were individually cloned into the BD vector at the *EcoRI* and *BamHI* sites with the same assembly mix. The resulting plasmids were transformed into yeast strain AH109. The yeast strain containing the segment of 1-130 AA showed no self-activation background in the test and was used as the bait for further Y2H screening using a 7 DAP maize kernel library from Hybrigenics Services, S.A.S., Evry, France.

The coding sequence for AA 1-130 of UFO1 (NM_001176801.1) was PCR-amplified and cloned into pB29 as an N-terminal fusion to LexA (UFO1-LexA) (Supplementary Table S9). The construct was checked by sequencing and used as bait to screen a random-primed *Z. mays* Kernel cDNA library constructed into pP6. pB29 was derived from the original pBTM116 vector (Vojtek and Hollenberg 1995; Béranger et al. 1997), and pP6 was based on the pGADGH plasmid (Bartel et al. 1993).

One hundred and eleven million clones (11-fold the complexity of the library) were screened using a mating approach with YHGX13 (Y187 ade2-101::loxP-kanMX-loxP, mata) and L40DGal4 (mata) yeast strains as previously described (Fromont-Racine et al. 1997). In total, 205 His + colonies were selected on a medium lacking tryptophan, leucine and histidine, and supplemented with 0.5 mM 3-Aminotriazol. The prey fragments of the positive clones were amplified by PCR and sequenced at their 5′ and 3′ junctions. The resulting sequences were used to identify the corresponding interacting proteins in the GenBank database (NCBI) using a fully automated procedure. A confidence score (PBS, for Predicted Biological Score) was attributed to each interaction as previously described (Formstecher et al. 2005).

Y2H 1by1 interaction assay

The 1by1 Y2H interaction assays were performed by Hybrigenics Services SAS, Evry, France (http://www.hybrigenics-services.com). The coding sequence for 1 to 130 AA of UFO1 (NM_001176801.1) was PCR-amplified and cloned into pB29 as an N-terminal fusion to LexA (UFO1-LexA. pB29 derives from the original pBTM116 vector (Vojtek and Hollenberg 1995; Béranger et al. 1997)). The fragments of the tested prey protein genes were extracted from the ULTImate Y2H screening of UFO1 with a random-primed *Z. mays* Kernel cDNA library. Prey fragments are cloned in frame with the Gal4 AD into plasmid pP6, derived from the original pGADGH (Bartel et al. 1993). The AD construct was checked by sequencing. Bait and prey constructs were transformed in the yeast haploid cells L40deltaGal4 (mata) and YHGX13 (Y187 ade2-101::loxP-kanMX-loxP, matα), respectively. The diploid yeast cells were obtained using a mating protocol with both yeast strains (Fromont-Racine et al. 1997). These assays are based on the HIS3 reporter gene (growth assay without histidine). As negative controls, the bait plasmid was tested in the presence of an empty prey vector (pP7) and all prey plasmids were tested with the empty bait vector (pB29). The interaction between SMAD and SMURF is used as the positive control (Colland et al. 2004). Controls and interactions were tested in the form of streaks of 3 independent yeast clones on DO-2 and DO-3 selective media. The DO-2 selective medium lacking tryptophan and leucine was used as a growth control and to verify the presence of the bait and prey plasmids. The DO-3 selective medium without tryptophan, leucine, and histidine selects for the interaction between bait and prey.

Luciferase complementation imaging

Primers were designed for amplifying candidate genes from the cDNA from the total RNA of kernels harvested at 6, 8, 16, and 18 DAP (Supplementary Table S10). The amplified genes were recombined in JW771 (35S LUC-N) and JW772 (35S LUC-C) vectors, transformed, and the resulting clones were confirmed. All constructs were introduced in Agrobacterium strain GV3101. The resulting colonies were grown in Luria-Bertani medium overnight at 28 °C. The next day, cells were pelleted by centrifugation and resuspended in infiltration buffer (10 mM of MES at pH 5.7, 10 mM of $MgCl_2$, and 150 μM of acetosyringone) to a final cell density corresponding to OD_{600} of 1.0 before infiltration into the leaves of 5-wk-old *N. benthamiana* plants. After growth for 48 h under a 16 h light/8 h dark photoperiod, the leaves were injected with 1 mM of luciferin (LUC), and the resulting LUC signal was captured using the Tanon-5200 image system. These experiments were repeated 3 times with similar results.

Protein expression and isolation

The complete coding sequence of ZmUFO1 with hexa histidine-tag was cloned in *E. coli*, expression vector pET-30a(+) and was transformed into the expression host, *E. coli* BL21 (DE3) (Novagen, Madison, WI, USA). Individual colony was inoculated into 50 ml Luria Broth (LB) medium (1% Bacto-tryptone, 0.5% yeast extract, and 8 mM NaCl) supplemented with 50 μg ml^{-1} kanamycin and cultured overnight at 37 °C in a shaker incubator. The fully grown cultures were mixed in 1 l LB medium with 50 μg ml^{-1} kanamycin. The culture was grown at 25 °C and IPTG (final concentration of 1 mM) was added when the OD_{600} reached 0.5. The cultures were harvested after 5 h and the cells were washed and resuspended in 30 ml equilibration buffer (50 mM Tris-HCl pH 8 + 300 mM NaCl + 5 mM imidazole; pH 8.0). The cells were lysed in the presence of 100 mM PMSF (working concentration 0.16 mM) and lysozyme (working concentration 0.2 mg ml^{-1}). The insoluble inclusion bodies were separated by centrifugation at 14,000 × *g* for 30 min at 4 °C. The His-tagged ZmUFO1 was purified by immobilized metal affinity chromatography (IMAC) using BD Talon Co^{2+} resin (Takara Bio Company, San Jose, CA, USA) and finally stored in 10 mM phosphate buffer.

Differential interference contrast

DIC imaging was performed on an Olympus BX61 microscope, equipped with a 63× oil immersion objective (Plan-Apochromat 63×/1.4 Oil DIC M27). For each condition, 3 replicates of 20 μl sample were prepared, incubated for 10 min, and imaged using a Nunc Lab-Tek Chambered Cover-glass (Thermo Fisher Scientific Inc, Waltham, MA, USA).

Dynamic light scattering

DLS measurements were conducted using a Wyatt Dynapro Nanostar DLS instrument (Wyatt Technology, Santa Barbara, CA, USA). Before analysis, samples underwent ultra-centrifugation at 15,000 rpm for 15 min to remove any large aggregates or impurities. A buffer offset was run before analyzing the samples to adjust for viscosity variations. For each measurement, 50 μl of the ZmUFO1 at a concentration of 0.8 mg ml^{-1} was loaded into a quartz cuvette and sealed with a cap to prevent contamination. The laser wavelength used was 660 nm, with detection at a 90° angle. Temperature increment experiments were conducted over a range of 4 to 40 °C and 4 to 80 °C, with temperature increments set to 0.5 °C. Data acquisition involved averaging over 5 acquisitions taken within a 5-s timeframe to ensure accuracy and reliability. Data analysis was performed using Dynamics software version 8.0.0.89 to derive relevant information regarding particle size distribution and dynamics.

CD spectroscopy

CD spectroscopy measurements were conducted using a JASCO J-1500 spectrometer (Jasco, Oklahoma City, OK, USA) equipped with a Peltier model PTC-517 thermostat cell holder. Signals were recorded across the wavelength range of 260 to 180 nm, with a scan speed of 50 nm min^{-1} and a bandwidth of 1 nm, maintained at a temperature of 20 °C. The path length of the quartz cell was set to 1 mm. The concentration of ZmUFO1 was determined to be 0.8 mg ml^{-1}. Before sample analysis, a buffer blank was run for baseline subtraction, and the resulting data were converted to units of molar ellipticity. Data analysis was performed using both the Jasco Multivariate SSE program and the BestSel single spectra analysis and fold recognition software (Micsonai et al. 2018).

Statistical analysis

Microsoft Excel version 16.16.25 was used for preparing graphs and standard error bars. Statistical analysis (paired *t*-test and one-way ANOVA with post-hoc Tukey's HSD test) was done using Microsoft Excel and R statistical package (Supplementary Data Set 2).

Accession numbers

Sequence of *ZmUfo1-1* with CACTA transposon, *MK288027*; *Zmufo1*, *Zm00001d000009* (GRMZM2G053177); *ufo1* orthologs: *Setaria italica*, LOC101754388, *Sorghum bicolor*, Sobic.007G066200 and Sobic.

007G066566, *Oryza sativa*, LOC_Os08g08880, and LOC_Os08g08900; RNA-Seq libraries (GEO accession number GSE117782; https://www.ncbi.nlm.nih.gov/geo/query/acc.cgi?acc=GSE117782 and https://www.ncbi.nlm.nih.gov/sra/SRP155527).

Acknowledgments

We thank Penn State Russel E. Larson farm, greenhouse, and Microscopy Core Facility staff for their assistance. We are grateful to Frederic Pontvianne, Cristina Rosa, Charles T. Anderson, and Julia Ann Fecko for guidance with subcellular localization, confocal microscopy, and protein-related experiments. We also thank the Bioinformatics Core Lab of the Institute of Plant and Microbial Biology, Academia Sinica, for the transcriptome analysis. We are grateful to Dr. Hong Ma for his valuable suggestions during the course of this research project. We are thankful for the suggestions and constructive criticisms of anonymous reviewers to improve this manuscript.

Author contributions

D.C., Z.Z., P.-Y.C., R.S., and S.C. designed experiments. D.C., Z.Z., P.-H.W., G.K.S., and S.C. performed experiments. D.C., Z.Z., P.-Y.L., P.-H.W., J.-W.A.H., and N.H.Y. analyzed data. B.C.M. maintained the databases. S.C. and B.C.M. obtained funding. D.C. and S.C. wrote the manuscript. D.C., Z.Z., P.-Y.L., P.-H.W., J.-W.A.H., P.-Y.C., R.S., B.C.M., N.H.Y., and S.C. edited the manuscript.

Supplementary data

The following materials are available in the online version of this article.

Supplementary Figure S1. *Zmufo1* mutants have abnormal raffinose levels.

Supplementary Figure S2. Abnormal reactive oxygen species accumulation, cell death, and DNA damage in *Zmufo1* mutants.

Supplementary Figure S3. In vitro exogenous antioxidant treatment of developing kernels restore normal expression of ROS and BETL-marker genes.

Supplementary Figure S4. Misregulation of *Zmufo1* affects the expression of essential genes for endosperm development and chromatin remodeling-related genes.

Supplementary Figure S5. Yeast two-hybrid (Y2H) screen using 10 days after pollination maize kernel Y2H library.

Supplementary Figure S6. Interacting protein partners of ZmUFO1.

Supplementary Figure S7. Predicted domains of interacting proteins of ZmUFO1.

Supplementary Figure S8. Dynamic light scattering result showing the distribution of ZmUFO1-His protein molecules in 3 distinct radius groups at different temperatures.

Supplementary Table S1. PAGE enriched GO (gene ontology) terms and Z-scores for significantly expressed GO terms for *Ufo1-1* 18 DAP pericarp (Wittmeyer et al. 2018; Chatterjee et al. 2021) and *P1-rr* 14 DAP pericarp (Morohashi et al. 2012) where positive Z-scores indicate the genes within a GO category are more upregulated on average, while negative values indicate downregulation.

Supplementary Table S2. ZmUFO1-interacting proteins identified by yeast (*Saccharomyces cerevisiae*) two-hybrid (Y2H) and yeast one-by-one assay.

Supplementary Table S3. Proteins interacting with ZmUFO1 and ZmUFO1$^{1\text{-}130AA}$ in luciferase complementation imaging (LCI) assay.

Supplementary Table S4. Primers used in the study for genotyping.

Supplementary Table S5. Primers used in the study for RT-qPCR-based expression assay.

Supplementary Table S6. Primers used for chromatin immunoprecipitation (ChIP) followed by RT-qPCR (ChIP-RT-qPCR) assay.

Supplementary Table S7. Primers used in the study to develop *pro35S:ZmUFO1-GFP* construct.

Supplementary Table S8. Primers used in the preliminary yeast (*Saccharomyces cerevisiae*) two-hybrid (Y2H) interaction assay.

Supplementary Table S9. Details of the development of ZmUFO1$^{1\text{-}130AA}$ bait for yeast (*Saccharomyces cerevisiae*) two-hybrid (Y2H) interaction assay.

Supplementary Table S10. Primers used in the luciferase complementation imaging (LCI) assay.

Supplementary Text S1. Predicted nature of ZmUFO1, its putative orthologs, and its interacting protein partners.

Supplementary Materials and Methods S1. Isolation of *U-E*, *U-S*, and WT near-isogenic lines.

Supplementary Materials and Methods S2. DNA extraction.

Supplementary Data Set 1. Expression ($\log_2$fold changes) and P-adjusted value of significantly differentially expressed genes in 10 DAP kernel transcriptome of *ufo1-Dsg* as compared with that of wild-type W22.

Supplementary Data Set 2. Summary of statistical analysis.

Funding

This work was supported by the National Science Foundation collaborative awards 1051654 to S.C., 1051576 to B.C.M., MCB-2341575 to S.C. and D.C., USDA/NIFA 2019-70006-30442, 2020-67013-31918, and AES Hatch awards PEN04613 and PEN04780 to S.C., the National Science and Technology Council Taiwan grant 109-2313-B-001-009-MY3 to P.-Y.C., and SIG S10 of the National Institutes of Health under award S10-OD030490-01 to N.H.Y. D.C. was supported by Netaji Subhas—Indian Council of Agricultural Research (ICAR) International Fellowship and a Graduate assistantship from the Department of Plant Science, Penn State University.

Conflict of interest statement: The authors declare no competing financial interests.

Data availability

The data underlying this article will be shared on reasonable request to the corresponding author.

References

Ageeva-Kieferle A, Rudolf EE, Lindermayr C. Redox-dependent chromatin remodeling: a new function of nitric oxide as architect of chromatin structure in plants. *Front Plant Sci*. 2019:10:625. https://doi.org/10.3389/fpls.2019.00625

Alexieva V, Sergiev I, Mapelli S, Karanov E. The effect of drought and ultraviolet radiation on growth and stress markers in pea and wheat. *Plant Cell Environ*. 2001:24(12):1337–1344. https://doi.org/10.1046/j.1365-3040.2001.00778.x

Andrews BJ, Lehman JA, Turchi JJ. Kinetic analysis of the Ku-DNA binding activity reveals a redox-dependent alteration in protein structure that stimulates dissociation of the Ku-DNA complex. *J Biol Chem*. 2006:281(19):13596–13603. https://doi.org/10.1074/jbc.M512787200

Andriunas FA, Zhang H-M, Xia X, Patrick JW, Offler CE. Intersection of transfer cells with phloem biology—broad evolutionary trends, function, and induction. *Front Plant Sci*. 2013:4:221. https://doi.org/10.3389/fpls.2013.00221

Baile F, Gómez-Zambrano Á, Calonje M. Roles of polycomb complexes in regulating gene expression and chromatin structure in plants. *Plant Commun*. 2022:3(1):100267. https://doi.org/10.1016/j.xplc.2021.100267

Bailly C, El-Maarouf-Bouteau H, Corbineau F. From intracellular signaling networks to cell death: the dual role of reactive oxygen species in seed physiology. *C R Biol*. 2008:331(10):806–814. https://doi.org/10.1016/j.crvi.2008.07.022

Barik A, Katuwawala A, Hanson J, Paliwal K, Zhou Y, Kurgan L. DEPICTER: intrinsic disorder and disorder function prediction server. *J Mol Biol*. 2020:432(11):3379–3387. https://doi.org/10.1016/j.jmb.2019.12.030

Barneche F, Steinmetz F, Echeverría M. Fibrillarin genes encode both a conserved nucleolar protein and a novel small nucleolar RNA involved in ribosomal RNA methylation in *Arabidopsis thaliana*. *J Biol Chem*. 2000:275(35):27212–27220. https://doi.org/10.1016/S0021-9258(19)61499-7

Bartel PL, Chein CT, Sternglanz R, Fields S. *Cellular interactions in development: a practical approach*. Oxford: Oxford University Press; 1993. p. 153–179.

Becraft PW. Cell fate specification in the cereal endosperm. *Semin Cell Dev Biol*. 2001:12(5):387–394. https://doi.org/10.1006/scdb.2001.0268

Becraft PW, Kang S-H, Suh S-G. The maize CRINKLY4 receptor kinase controls a cell-autonomous differentiation response. *Plant Physiol*. 2001:127(2):486–496. https://doi.org/10.1104/pp.010299

Bellegarde F, Maghiaoui A, Boucherez J, Krouk G, Lejay L, Bach L, Gojon A, Martin A. The chromatin factor HNI9 and ELONGATED HYPOCOTYL5 maintain ROS homeostasis under high nitrogen provision. *Plant Physiol*. 2019:180(1):582–592. https://doi.org/10.1104/pp.18.01473

Béranger F, Aresta S, de Gunzburg J, Camonis J. Getting more from the two-hybrid system: N-terminal fusions to LexA are efficient and sensitive baits for two-hybrid studies. *Nucleic Acids Res*. 1997:25(10):2035–2036. https://doi.org/10.1093/nar/25.10.2035

Berg A, de Kok A. 2-Oxo acid dehydrogenase multienzyme complexes. The central role of the lipoyl domain. *Biol Chem*. 1997:378(7):617–634.

Bethke PC, Jones RL. Cell death of barley aleurone protoplasts is mediated by reactive oxygen species. *Plant J*. 2001:25(1):19–29. https://doi.org/10.1111/j.1365-313X.2001.00930.x

Bieluszewski T, Sura W, Dziegielewski W, Bieluszewska A, Lachance C, Kabza M, Szymanska-Lejman M, Abram M, Wlodzimierz P, De Winne N, et al. Nua4 and H2A.Z control environmental responses and autotrophic growth in Arabidopsis. *Nat Commun*. 2022:13(1):277. https://doi.org/10.1038/s41467-021-27882-5

Boros J, Arnoult N, Stroobant V, Collet J-F, Decottignies A. Polycomb repressive complex 2 and H3K27me3 cooperate with H3K9 methylation to maintain heterochromatin protein 1α at chromatin. *Mol Cell Biol*. 2014:34(19):3662–3674. https://doi.org/10.1128/MCB.00205-14

Brown SH, Yarden O, Gollop N, Chen S, Zveibil A, Belausov E, Freeman S. Differential protein expression in *Colletotrichum acutatum*: changes associated with reactive oxygen species and nitrogen starvation implicated in pathogenicity on strawberry. *Mol Plant Pathol*. 2008:9(2):171–190. https://doi.org/10.1111/j.1364-3703.2007.00454.x

Carmo-Fonseca M, Mendes-Soares L, Campos I. To be or not to be in the nucleolus. *Nat Cell Biol*. 2000:2(6):107–112. https://doi.org/10.1038/35014078

Casati P, Gomez MS. Chromatin dynamics during DNA damage and repair in plants: new roles for old players. *J Exp Bot*. 2021:72(11):4119–4131. https://doi.org/10.1093/jxb/eraa551

Cervera AM, Bayley J-P, Devilee P, McCreath KJ. Inhibition of succinate dehydrogenase dysregulates histone modification in mammalian cells. *Mol Cancer*. 2009:8(1):89. https://doi.org/10.1186/1476-4598-8-89

Chatterjee D, Wittmeyer K, Lee T-F, Cui J, Yennawar NH, Yennawar HP, Meyers BC, Chopra S. Maize *unstable factor for orange1* is essential for endosperm development and carbohydrate accumulation. *Plant Physiol*. 2021:186(4):1932–1950. https://doi.org/10.1093/plphys/kiab183

Chen C, Li C, Wang Y, Renaud J, Tian G, Kambhampati S, Saatian B, Nguyen V, Hannoufa A, Marsolais F, et al. Cytosolic acetyl-CoA promotes histone acetylation predominantly at H3K27 in Arabidopsis. *Nat Plants*. 2017a:3(10):814–824. https://doi.org/10.1038/s41477-017-0023-7

Chen J, Yang S, Fan B, Zhu C, Chen Z. The mediator complex: a central coordinator of plant adaptive responses to environmental stresses. *Int J Mol Sci*. 2022:23(11):6170. https://doi.org/10.3390/ijms23116170

Chen J, Zeng B, Zhang M, Xie S, Wang G, Hauck A, Lai J. Dynamic transcriptome landscape of maize embryo and endosperm development. *Plant Physiol*. 2014:166(1):252–264. https://doi.org/10.1104/pp.114.240689

Chen X, Feng F, Qi W, Xu L, Yao D, Wang Q, Song R. *Dek35* encodes a PPR protein that affects *cis*-splicing of mitochondrial *nad4* intron 1 and seed development in maize. *Mol Plant*. 2017b:10(3):427–441. https://doi.org/10.1016/j.molp.2016.08.008

Cheng W-H, Chourey PS. Genetic evidence that invertase-mediated release of hexoses is critical for appropriate carbon partitioning and normal seed development in maize. *Theor Appl Genet*. 1999:98(3–4):485–495. https://doi.org/10.1007/s001220051096

Cheng XX, Yu M, Zhang N, Zhou ZQ, Xu QT, Mei FZ, Qu LH. Reactive oxygen species regulate programmed cell death progress of endosperm in winter wheat (*Triticum aestivum* L.) under waterlogging. *Protoplasma*. 2016:253(2):311–327. https://doi.org/10.1007/s00709-015-0811-8

Chittuluru JR, Chaban Y, Monnet-Saksouk J, Carrozza MJ, Sapountzi V, Selleck W, Huang J, Utley RT, Cramet M, Allard S, et al. Structure and nucleosome interaction of the yeast NuA4 and Piccolo-NuA4 histone acetyltransferase complexes. *Nat Struct Mol Biol*. 2011:18(11):1196–1203. https://doi.org/10.1038/nsmb.2128

Cho S-H, Lee C-H, Gi E, Yim Y, Koh H-J, Kang K, Paek N-C. The rice rolled fine striped (RFS) CHD3/Mi-2 chromatin remodeling factor epigenetically regulates genes involved in oxidative stress responses during leaf development. *Front Plant Sci*. 2018:9:364. https://doi.org/10.3389/fpls.2018.00364

Chopra S, Cocciolone SM, Bushman S, Sangar V, McMullen MD, Peterson T. The maize *unstable factor for orange1* is a dominant epigenetic modifier of a tissue specifically silent allele of *pericarp color1*. *Genetics*. 2003:163(3):1135–1146. https://doi.org/10.1093/genetics/163.3.1135

Chourey PS, Hueros G. The basal endosperm transfer layer (BETL): gateway to the maize kernel. In: *Maize kernel development*. Wallingford, UK: CABI; 2017. p. 56–67. https://doi.org/10.1079/9781786391216.0056

Cmarko D, Verschure PJ, Otte AP, van Driel R, Fakan S. Polycomb group gene silencing proteins are concentrated in the perichromatin compartment of the mammalian nucleus. *J Cell Sci*. 2003:116(2):335–343. https://doi.org/10.1242/jcs.00225

Colland F, Jacq X, Trouplin V, Mougin C, Groizeleau C, Hamburger A, Meil A, Wojcik J, Legrain P, Gauthier J-M. Functional proteomics mapping of a human signaling pathway. *Genome Res*. 2004:14(7): 1324–1332. https://doi.org/10.1101/gr.2334104

Condori-Apfata JA, Batista-Silva W, Medeiros DB, Vargas JR, Valente LML, Heyneke E, Pérez-Diaz JL, Fernie AR, Araújo WL, Nunes-Nesi A. The Arabidopsis E(1) subunit of the 2-oxoglutarate dehydrogenase complex modulates plant growth and seed production. *Plant Mol Biol*. 2019:101(1–2):183–202. https://doi.org/10.1007/s11103-019-00900-3

Considine MJ, Foyer CH. Redox regulation of plant development. *Antioxid Redox Signal*. 2014:21(9):1305–1326. https://doi.org/10.1089/ars.2013.5665

Considine MJ, Goodman M, Echtay KS, Laloi M, Whelan J, Brand MD, Sweetlove LJ. Superoxide stimulates a proton leak in potato mitochondria that is related to the activity of uncoupling protein. *J Biol Chem*. 2003:278(25):22298–22302. https://doi.org/10.1074/jbc.M301075200

Crevillén P, Gómez-Zambrano Á, López JA, Vázquez J, Piñeiro M, Jarillo JA. Arabidopsis YAF9 histone readers modulate flowering time through NuA4-complex-dependent H4 and H2A.Z histone acetylation at FLC chromatin. *New Phytol*. 2019:222(4):1893–1908. https://doi.org/10.1111/nph.15737

Dai D, Ma Z, Song R. Maize endosperm development. *J Integr Plant Biol*. 2021:63(4):613–627. https://doi.org/10.1111/jipb.13069

Dai D, Mudunkothge JS, Galli M, Char SN, Davenport R, Zhou X, Gustin JL, Spielbauer G, Zhang J, Barbazuk WB, et al. Paternal imprinting of *dosage-effect defective1* contributes to seed weight xenia in maize. *Nat Commun*. 2022:13(1):5366. https://doi.org/10.1038/s41467-022-33055-9

D'Arcy S, Luger K. Understanding histone acetyltransferase Rtt109 structure and function: how many chaperones does it take? *Curr Opin Struct Biol*. 2011:21(6):728–734. https://doi.org/10.1016/j.sbi.2011.09.005

Davies HG. Electron-microscope observations on the organization of heterochromatin in certain cells. *J Cell Sci*. 1968:3(1):129–150. https://doi.org/10.1242/jcs.3.1.129

De GuZman RN, Wojciak JM, Martinez-Yamout MA, Dyson HJ, Wright PE. CBP/p300 TAZ1 domain forms a structured scaffold for ligand binding. *Biochemistry*. 2005:44(2):490–497. https://doi.org/10.1021/bi048161t

Dibley SJ, Zhou Y, Andriunas FA, Talbot MJ, Offler CE, Patrick JW, McCurdy DW. Early gene expression programs accompanying trans-differentiation of epidermal cells of *Vicia faba* cotyledons into transfer cells. *New Phytol*. 2009:182(4):863–877. https://doi.org/10.1111/j.1469-8137.2009.02822.x

Dietz K-J, Mittler R, Noctor G. Recent progress in understanding the role of reactive oxygen species in plant cell signaling. *Plant Physiol*. 2016:171(3):1535–1539. https://doi.org/10.1104/pp.16.00938

Dobin A, Davis CA, Schlesinger F, Drenkow J, Zaleski C, Jha S, Batut P, Chaisson M, Gingeras TR. STAR: ultrafast universal RNA-Seq aligner. *Bioinformatics*. 2013:29(1):15–21. https://doi.org/10.1093/bioinformatics/bts635

Dolan WL, Dilkes BP, Stout JM, Bonawitz ND, Chapple C. Mediator complex subunits MED2, MED5, MED16, and MED23 genetically interact in the regulation of phenylpropanoid biosynthesis. *Plant Cell*. 2017:29(12):3269–3285. https://doi.org/10.1105/tpc.17.00282

Doll NM, Depege-Fargeix N, Rogowsky PM, Widiez T. Signaling in early maize kernel development. *Mol Plant*. 2017:10(3):375–388. https://doi.org/10.1016/j.molp.2017.01.008

Doll NM, Just J, Brunaud V, Caïus J, Grimault A, Depège-Fargeix N, Esteban E, Pasha A, Provart NJ, Ingram GC, et al. Transcriptomics at maize embryo/endosperm interfaces identifies a transcriptionally distinct endosperm subdomain adjacent to the embryo scutellum. *Plant Cell*. 2020:32(4):833–852. https://doi.org/10.1105/tpc.19.00756

Drozdowicz YM, Jones RL. Hormonal regulation of organic and phosphoric acid release by barley aleurone layers and scutella. *Plant Physiol*. 1995:108(2):769–776. https://doi.org/10.1104/pp.108.2.769

Du Z-Y, Chen M-X, Chen Q-F, Xiao S, Chye M-L. Overexpression of Arabidopsis acyl-CoA-binding protein ACBP2 enhances drought tolerance. *Plant Cell Environ*. 2013:36(2):300–314. https://doi.org/10.1111/j.1365-3040.2012.02574.x

Dyson HJ, Wright PE. Role of intrinsic protein disorder in the function and interactions of the transcriptional coactivators CREB-binding protein (CBP) and p300. *J Biol Chem*. 2016:291(13):6714–6722. https://doi.org/10.1074/jbc.R115.692020

Engelhorn J, Blanvillain R, Carles CC. Gene activation and cell fate control in plants: a chromatin perspective. *Cell Mol Life Sci*. 2014:71(16):3119–3137. https://doi.org/10.1007/s00018-014-1609-0

Espinosa-Cores L, Bouza-Morcillo L, Barrero-Gil J, Jiménez-Suárez V, Lázaro A, Piqueras R, Jarillo JA, Piñeiro M. Insights into the function of the NuA4 complex in plants. *Front Plant Sci*. 2020:11:125. https://doi.org/10.3389/fpls.2020.00125

Fan K, Ren Z, Zhang X, Liu Y, Fu J, Qi C, Tatar W, Rasmusson AG, Wang G, Liu Y. The pentatricopeptide repeat protein EMP603 is required for the splicing of mitochondrial *Nad1* intron 2 and seed development in maize. *J Exp Bot*. 2021:72(20):6933–6948. https://doi.org/10.1093/jxb/erab339

Fina JP, Masotti F, Rius SP, Crevacuore F, Casati P. HAC1 and HAF1 histone acetyltransferases have different roles in UV-B responses in Arabidopsis. *Front Plant Sci*. 2017:8:1179. https://doi.org/10.3389/fpls.2017.01179

Fomenko DE, Gladyshev VN. Identity and functions of CxxC-derived motifs. *Biochemistry*. 2003:42(38):11214–11225. https://doi.org/10.1021/bi034459s

Fomenko DE, Xing W, Adair BM, Thomas DJ, Gladyshev VN. High-throughput identification of catalytic redox-active cysteine residues. *Science*. 2007:315(5810):387–389. https://doi.org/10.1126/science.1133114

Formstecher E, Aresta S, Collura V, Hamburger A, Meil A, Trehin A, Reverdy C, Betin V, Maire S, Brun C, et al. Protein interaction mapping: a Drosophila case study. *Genome Res*. 2005:15(3):376–384. https://doi.org/10.1101/gr.2659105

Foyer CH, Wilson MH, Wright MH. Redox regulation of cell proliferation: bioinformatics and redox proteomics approaches to identify redox-sensitive cell cycle regulators. *Free Radic Biol Med*. 2018:122: 137–149. https://doi.org/10.1016/j.freeradbiomed.2018.03.047

Fromont-Racine M, Rain JC, Legrain P. Toward a functional analysis of the yeast genome through exhaustive two-hybrid screens. *Nat Genet*. 1997:16(3):277–282. https://doi.org/10.1038/ng0797-277

Fujita H, Fujii R, Aratani S, Amano T, Fukamizu A, Nakajima T. Antithetic effects of MBD2a on gene regulation. *Mol Cell Biol*. 2003: 23(8):2645–2657. https://doi.org/10.1128/MCB.23.8.2645-2657.2003

Galarneau L, Nourani A, Boudreault AA, Zhang Y, Héliot L, Allard S, Savard J, Lane WS, Stillman DJ, Côté J. Multiple links between the NuA4 histone acetyltransferase complex and epigenetic control of transcription. *Mol Cell*. 2000:5(6):927–937. https://doi.org/10.1016/S1097-2765(00)80258-0

Galdieri L, Vancura A. Acetyl-CoA carboxylase regulates global histone acetylation. *J Biol Chem*. 2012:287(28):23865–23876. https://doi.org/10.1074/jbc.M112.380519

Groth M, Moissiard G, Wirtz M, Wang H, Garcia-Salinas C, Ramos-Parra PA, Bischof S, Feng S, Cokus SJ, John A, et al. MTHFD1 controls DNA methylation in Arabidopsis. *Nat Commun*. 2016:7(1): 11640. https://doi.org/10.1038/ncomms11640

Guo Y, Zhao S, Wang GG. Polycomb gene silencing mechanisms: PRC2 chromatin targeting, H3K27me3 'readout', and phase separation-based compaction. *Trends Genet*. 2021:37(6):547–565. https://doi.org/10.1016/j.tig.2020.12.006

Gutiérrez-Marcos JF, Dal Prà M, Giulini A, Costa LM, Gavazzi G, Cordelier S, Sellam O, Tatout C, Paul W, Perez P, et al. Empty pericarp4 encodes a mitochondrion-targeted pentatricopeptide repeat protein necessary for seed development and plant growth in maize. *Plant Cell*. 2007:19(1):196–210. https://doi.org/10.1105/tpc.105.039594

Haring M, Offermann S, Danker T, Horst I, Peterhansel C, Stam M. Chromatin immunoprecipitation: optimization, quantitative analysis and data normalization. *Plant Methods*. 2007:3(1):11. https://doi.org/10.1186/1746-4811-3-11

Haynes W. Benjamini-Hochberg method. In: Dubitzky W, Wolkenhauer O, Cho K-H, Yokota H, editors. *Encyclopedia of systems biology*. New York, NY: Springer; 2013. p. 78–78.

Hirsch CD, Springer NM. Transposable element influences on gene expression in plants. *Biochim Biophys Acta Gene Regul Mech*. 2017:1860(1):157–165. https://doi.org/10.1016/j.bbagrm.2016.05.010

Hoopes GM, Hamilton JP, Wood JC, Esteban E, Pasha A, Vaillancourt B, Provart NJ, Buell CR. An updated gene atlas for maize reveals organ-specific and stress-induced genes. *Plant J*. 2019:97(6): 1154–1167. https://doi.org/10.1111/tpj.14184

Hu M, Zhao H, Yang B, Yang S, Liu H, Tian H, Shui G, Chen Z, Lizhu E, Lai J, et al. *ZmCTLP1* is required for the maintenance of lipid homeostasis and the basal endosperm transfer layer in maize kernels. *New Phytol*. 2021:232(6):2384–2399. https://doi.org/10.1111/nph.17754

Huang H, Ullah F, Zhou DX, Yi M, Zhao Y. Mechanisms of ROS regulation of plant development and stress responses. *Front Plant Sci*. 2019:10:800. https://doi.org/10.3389/fpls.2019.00800

Huang X, Chen S, Li W, Tang L, Zhang Y, Yang N, Zou Y, Zhai X, Xiao N, Liu W, et al. ROS regulated reversible protein phase separation synchronizes plant flowering. *Nat Chem Biol*. 2021:17(5):549–557. https://doi.org/10.1038/s41589-021-00739-0

Jardim-Messeder D, Caverzan A, Rauber R, de Souza Ferreira E, Margis-Pinheiro M, Galina A. Succinate dehydrogenase (mitochondrial complex II) is a source of reactive oxygen species in plants and regulates development and stress responses. *New Phytol*. 2015:208(3):776–789. https://doi.org/10.1111/nph.13515

Jarosz M, Van Lijsebettens M, Woloszynska M. Plant elongator—protein complex of diverse activities regulates growth, development, and immune responses. *Int J Mol Sci*. 2020:21(18):6912. https://doi.org/10.3390/ijms21186912

Jefferson RA, Kavanagh TA, Bevan MW. GUS fusions: beta-glucuronidase as a sensitive and versatile gene fusion marker in higher plants. *EMBO J*. 1987:6(13):3901–3907. https://doi.org/10.1002/j.1460-2075.1987.tb02730.x

Kalinina NO, Makarova S, Makhotenko A, Love AJ, Taliansky M. The multiple functions of the nucleolus in plant development, disease and stress responses. *Front Plant Sci*. 2018:9:132. https://doi.org/10.3389/fpls.2018.00132

Kang B-H, Xiong Y, Williams DS, Pozueta-Romero D, Chourey PS. Miniature1-encoded cell wall invertase is essential for assembly and function of wall-in-growth in the maize endosperm transfer cell. *Plant Physiol*. 2009:151(3):1366–1376. https://doi.org/10.1104/pp.109.142331

Katsuya-Gaviria K, Caro E, Carrillo-Barral N, Iglesias-Fernández R. Reactive oxygen species (ROS) and nucleic acid modifications during seed dormancy. *Plants (Basel)*. 2020:9(6):679. https://doi.org/10.3390/plants9060679

Kelly RD, Parmar G, Bayat L, Maitland ERM, Lajoie GA, Edgell DR, Schild-Poulter C. Noncanonical functions of Ku may underlie essentiality in human cells. *Sci Rep*. 2023:13(1):12162. https://doi.org/10.1038/s41598-023-39166-7

Kimura H, Hayashi-Takanaka Y, Goto Y, Takizawa N, Nozaki N. The organization of histone H3 modifications as revealed by a panel of specific monoclonal antibodies. *Cell Struct Funct*. 2008:33(1):61–73. https://doi.org/10.1247/csf.07035

Kowles RV, Phillips RL. DNA amplification patterns in maize endosperm nuclei during kernel development. *Proc Natl Acad Sci U S A*. 1985:82(20):7010–7014. https://doi.org/10.1073/pnas.82.20.7010

Kowles RV, Phillips RL. Endosperm development in maize. *Int Rev Cytol*. 1988:112:97–136. https://doi.org/10.1016/S0074-7696(08)62007-0

Latrasse D, Benhamed M, Henry Y, Domenichini S, Kim W, Zhou DX, Delarue M. The MYST histone acetyltransferases are essential for gametophyte development in Arabidopsis. *BMC Plant Biol*. 2008:8(1): 121. https://doi.org/10.1186/1471-2229-8-121

Lavarone E, Barbieri CM, Pasini D. Dissecting the role of H3K27 acetylation and methylation in PRC2 mediated control of cellular identity. *Nat Commun*. 2019:10(1):1679. https://doi.org/10.1038/s41467-019-09624-w

Leach KA, Braun DM. Soluble sugar and starch extraction and quantification from maize (*Zea mays*) leaves. *Curr Protoc Plant Biol*. 2016:1(1):139–161. https://doi.org/10.1002/cppb.20018

LeClere S, Schmelz EA, Chourey PS. Cell wall invertase-deficient miniature1 kernels have altered phytohormone levels. *Phytochemistry*. 2008:69(3):692–699. https://doi.org/10.1016/j.phytochem.2007.09.011

LeClere S, Schmelz EA, Chourey PS. Sugar levels regulate tryptophan-dependent auxin biosynthesis in developing maize kernels. *Plant Physiol*. 2010:153(1):306–318. https://doi.org/10.1104/pp.110.155226

Leroux BM, Goodyke AJ, Schumacher KI, Abbott CP, Clore AM, Yadegari R, Larkins BA, Dannenhoffer JM. Maize early endosperm growth and development: from fertilization through cell type differentiation. *Am J Bot*. 2014:101(8):1259–1274. https://doi.org/10.3732/ajb.1400083

Li E, Liu H, Huang L, Zhang X, Dong X, Song W, Zhao H, Lai J. Long-range interactions between proximal and distal regulatory regions in maize. *Nat Commun*. 2019:10(1):2633. https://doi.org/10.1038/s41467-019-10603-4

Li G, Wang D, Yang R, Logan K, Chen H, Zhang S, Skaggs MI, Lloyd A, Burnett WJ, Laurie JD, et al. Temporal patterns of gene expression in developing maize endosperm identified through transcriptome sequencing. *Proc Natl Acad Sci U S A*. 2014:111(21):7582–7587. https://doi.org/10.1073/pnas.1406383111

Lindermayr C, Rudolf EE, Durner J, Groth M. Interactions between metabolism and chromatin in plant models. *Mol Metab*. 2020:38: 100951. https://doi.org/10.1016/j.molmet.2020.01.015

Linka N, Esser C. Transport proteins regulate the flux of metabolites and cofactors across the membrane of plant peroxisomes. *Front Plant Sci*. 2012:3:3. https://doi.org/10.3389/fpls.2012.00003

Lisch D. Epigenetic regulation of transposable elements in plants. *Annu Rev Plant Biol*. 2009:60(1):43–66. https://doi.org/10.1146/annurev.arplant.59.032607.092744

Lozano GM, Bejarano I, Espino J, González D, Ortiz A, García JF, Rodríguez AB, Pariente JA. Relationship between caspase activity and apoptotic markers in human sperm in response to hydrogen peroxide and progesterone. *J Reprod Dev*. 2009:55(6):615–621. https://doi.org/10.1262/jrd.20250

Ma S, Yang W, Liu X, Li S, Li Y, Zhu J, Zhang C, Lu X, Zhou X, Chen R. Pentatricopeptide repeat protein CNS1 regulates maize mitochondrial complex III assembly and seed development. *Plant Physiol*. 2022:189(2):611–627. https://doi.org/10.1093/plphys/kiac086

Margaria P, Anderson CT, Turina M, Rosa C. Identification of *Ourmiavirus* 30 K movement protein amino acid residues involved in symptomatology, viral movement, subcellular localization and tubule formation. *Mol Plant Pathol*. 2016:17(7):1063–1079. https://doi.org/10.1111/mpp.12348

Matuleviciute R, Cunha PP, Johnson RS, Foskolou IP. Oxygen regulation of TET enzymes. *FEBS J*. 2021:288(24):7143–7161. https://doi.org/10.1111/febs.15695

Maulión E, Gomez MS, Bustamante CA, Casati P. AtCAF-1 mutants show different DNA damage responses after ultraviolet-B than those activated by other genotoxic agents in leaves. *Plant Cell Environ*. 2019:42(9):2730–2745. https://doi.org/10.1111/pce.13596

McCarthy DJ, Chen Y, Smyth GK. Differential expression analysis of multifactor RNA-Seq experiments with respect to biological variation. *Nucleic Acids Res*. 2012:40(10):4288–4297. https://doi.org/10.1093/nar/gks042

McCurdy DW, Hueros G. Transfer cells. *Front Plant Sci*. 2014:5:672. https://doi.org/10.3389/fpls.2014.00672

Meng W, Xu L, Du ZY, Wang F, Zhang R, Song X, Lam SM, Shui G, Li Y, Chye M-L. RICE ACYL-COA-BINDING PROTEIN6 affects Acyl-CoA homeostasis and growth in rice. *Rice (N Y)*. 2020:13(1):75. https://doi.org/10.1186/s12284-020-00435-y

Mészáros B, Erdos G, Dosztányi Z. IUPred2A: context-dependent prediction of protein disorder as a function of redox state and protein binding. *Nucleic Acids Res*. 2018:46(W1):W329–W337. https://doi.org/10.1093/nar/gky384

Mhamdi A, Van Breusegem F. Reactive oxygen species in plant development. *Development*. 2018:145(15):dev164376. https://doi.org/10.1242/dev.164376

Micsonai A, Wien F, Bulyáki É, Kun J, Moussong É, Lee YH, Goto Y, Réfrégiers M, Kardos J. BeStSel: a web server for accurate protein secondary structure prediction and fold recognition from the circular dichroism spectra. *Nucleic Acids Res*. 2018:46(W1):W315–W322. https://doi.org/10.1093/nar/gky497

Mitchell L, Huard S, Cotrut M, Pourhanifeh-Lemeri R, Steunou A-L, Hamza A, Lambert J-P, Zhou H, Ning Z, Basu A, et al. mChIP-KAT-MS, a method to map protein interactions and acetylation sites for lysine acetyltransferases. *Proc Natl Acad Sci U S A*. 2013:110(17):1641–1650. https://doi.org/10.1073/pnas.1218515110

Mittler R, Vanderauwera S, Suzuki N, Miller G, Tognetti VB, Vandepoele K, Gollery M, Shulaev V, Van Breusegem F. ROS signaling: the new wave? *Trends Plant Sci*. 2011:16(6):300–309. https://doi.org/10.1016/j.tplants.2011.03.007

Morohashi K, Casas MI, Falcone-Ferreyra ML, Mejía-Guerra MK, Pourcel L, Yilmaz A, Feller A, Carvalho B, Emiliani J, Rodriguez E, et al. A genome-wide regulatory framework identifies maize *pericarp color1* controlled genes. *Plant Cell*. 2012:24(7):2745–2764. https://doi.org/10.1105/tpc.112.098004

Neufeld TP. TOR-dependent control of autophagy: biting the hand that feeds. *Curr Opin Cell Biol*. 2010:22(2):157–168. https://doi.org/10.1016/j.ceb.2009.11.005

Nishizawa-Yokoi A, Yabuta Y, Shigeoka S. The contribution of carbohydrates including raffinose family oligosaccharides and sugar alcohols to protection of plant cells from oxidative damage. *Plant Signal Behav*. 2008:3(11):1016–1018. https://doi.org/10.4161/psb.6738

Offler CE, McCurdy DW, Patrick JW, Talbot MJ. Transfer cells: cells specialized for a special purpose. *Annu Rev Plant Biol*. 2003:54(1):431–454. https://doi.org/10.1146/annurev.arplant.54.031902.134812

Offler CE, Patrick JW. Transfer cells: what regulates the development of their intricate wall labyrinths? *New Phytol*. 2020:228(2):427–444. https://doi.org/10.1111/nph.16707

Ojolo SP, Cao S, Priyadarshani SVGN, Li W, Yan M, Aslam M, Zhao H, Qin Y. Regulation of plant growth and development: a review from a chromatin remodeling perspective. *Front Plant Sci*. 2018:9:1232. https://doi.org/10.3389/fpls.2018.01232

Olsen O-A. ENDOSPERM DEVELOPMENT: cellularization and cell fate specification. *Annu Rev Plant Physiol Plant Mol Biol*. 2001:52(1):233–267. https://doi.org/10.1146/annurev.arplant.52.1.233

Panikulangara TJ, Eggers-Schumacher G, Wunderlich M, Stransky H, Schöffl F. Galactinol synthase1. A novel heat shock factor target gene responsible for heat-induced synthesis of raffinose family oligosaccharides in Arabidopsis. *Plant Physiol*. 2004:136(2):3148–3158. https://doi.org/10.1104/pp.104.042606

Pontvianne F, Blevins T, Chandrasekhara C, Mozgová I, Hassel C, Pontes OM, Tucker S, Mokros P, Muchová V, Fajkus J, et al. Subnuclear partitioning of rRNA genes between the nucleolus and nucleoplasm reflects alternative epiallelic states. *Genes Dev*. 2013:27(14):1545–1550. https://doi.org/10.1101/gad.221648.113

Pu Y, Luo X, Bassham DC. TOR-dependent and -independent pathways regulate autophagy in *Arabidopsis thaliana*. *Front Plant Sci*. 2017:8:1204. https://doi.org/10.3389/fpls.2017.01204

Qi W, Zhu J, Wu Q, Wang Q, Li X, Yao D, Jin Y, Wang G, Wang G, Song R. Maize *reas1* mutant stimulates ribosome use efficiency and triggers distinct transcriptional and translational responses. *Plant Physiol*. 2016:170(2):971–988. https://doi.org/10.1104/pp.15.01722

Questa JI, Rius SP, Casadevall R, Casati P. ZmMBD101 is a DNA-binding protein that maintains Mutator elements chromatin in a repressive state in maize. *Plant Cell Environ*. 2016:39(1):174–184. https://doi.org/10.1111/pce.12604

Ren RC, Lu X, Zhao YJ, Wei YM, Wang LL, Zhang L, Zhang WT, Zhang C, Zhang XS, Zhao XY. Pentatricopeptide repeat protein DEK40 is required for mitochondrial function and kernel development in maize. *J Exp Bot*. 2019:70(21):6163–6179. https://doi.org/10.1093/jxb/erz391

Robin M, Issa AR, Santos CC, Napoletano F, Petitgas C, Chatelain G, Ruby M, Walter L, Birman S, Domingos PM, et al. Drosophila p53 integrates the antagonism between autophagy and apoptosis in response to stress. *Autophagy*. 2019:15(5):771–784. https://doi.org/10.1080/15548627.2018.1558001

Robinson MD, McCarthy DJ, Smyth GK. Edger: a Bioconductor package for differential expression analysis of digital gene expression data. *Bioinformatics*. 2010:26(1):139–140. https://doi.org/10.1093/bioinformatics/btp616

Rübe CE, Lorat Y, Schuler N, Schanz S, Wennemuth G, Rübe C. DNA repair in the context of chromatin: new molecular insights by the nanoscale detection of DNA repair complexes using transmission electron microscopy. *DNA Repair (Amst)*. 2011:10(4):427–437. https://doi.org/10.1016/j.dnarep.2011.01.012

Ryan CM, Harries JC, Kindle KB, Collins HM, Heery DM. Functional interaction of CREB binding protein (CBP) with nuclear transport proteins and modulation by HDAC inhibitors. *Cell Cycle*. 2006:5(18):2146–2152. https://doi.org/10.4161/cc.5.18.3207

Schippers JHM, Foyer CH, van Dongen JT. Redox regulation in shoot growth, SAM maintenance and flowering. *Curr Opin Plant Biol*. 2016:29:121–128. https://doi.org/10.1016/j.pbi.2015.11.009

Schmidt R, Schippers JHM. ROS-mediated redox signaling during cell differentiation in plants. *Biochim Biophys Acta*. 2015:1850(8): 1497–1508. https://doi.org/10.1016/j.bbagen.2014.12.020

Scott MS, Boisvert FM, McDowall MD, Lamond AI, Barton GJ. Characterization and prediction of protein nucleolar localization sequences. *Nucleic Acids Res*. 2010:38(21):7388–7399. https://doi.org/10.1093/nar/gkq653

Scott MS, Troshin PV, Barton GJ. Nod: a nucleolar localization sequence detector for eukaryotic and viral proteins. *BMC Bioinformatics*. 2011:12(1):317. https://doi.org/10.1186/1471-2105-12-317

Searle NE, Torres-Machorro AL, Pillus L. Chromatin regulation by the NuA4 acetyltransferase complex is mediated by essential interactions between enhancer of polycomb (*Epl1*) and *Esa1*. *Genetics*. 2017:205(3):1125–1137. https://doi.org/10.1534/genetics.116.197830

Sekhon RS, Chopra S. Progressive loss of DNA methylation releases epigenetic gene silencing from a tandemly repeated maize Myb gene. *Genetics*. 2009:181(1):81–91. https://doi.org/10.1534/genetics.108.097170

Sengupta S, Mukherjee S, Basak P, Majumder AL. Significance of galactinol and raffinose family oligosaccharide synthesis in plants. *Front Plant Sci*. 2015:6:656. https://doi.org/10.3389/fpls.2015.00656

Shen Y, Issakidis-Bourguet E, Zhou D-X. Perspectives on the interactions between metabolism, redox, and epigenetics in plants. *J Exp Bot*. 2016:67(18):5291–5300. https://doi.org/10.1093/jxb/erw310

Snape A. MBDs mediate methylation, deacetylation and transcriptional repression. *Trends Genet*. 2000:16(1):20. https://doi.org/10.1016/S0168-9525(99)01925-3

Sosso D, Luo D, Li QB, Sasse J, Yang J, Gendrot G, Suzuki M, Koch KE, McCarty DR, Chourey PS, et al. Seed filling in domesticated maize and rice depends on SWEET-mediated hexose transport. *Nat Genet*. 2015:47(12):1489–1493. https://doi.org/10.1038/ng.3422

Stenström L, Mahdessian D, Gnann C, Cesnik AJ, Ouyang W, Leonetti MD, Uhlén M, Cuylen-Haering S, Thul PJ, Lundberg E. Mapping the nucleolar proteome reveals a spatiotemporal organization related to intrinsic protein disorder. *Mol Syst Biol*. 2020:16(8):e9469. https://doi.org/10.15252/msb.20209469

Suski JM, Lebiedzinska M, Bonora M, Pinton P, Duszynski J, Wieckowski MR. Relation between mitochondrial membrane potential and ROS formation. *Methods Mol Biol*. 2012:810:183–205. https://doi.org/10.1007/978-1-61779-382-0_12

Talbot MJ, Offler CE, McCurdy DW. Transfer cell wall architecture: a contribution towards understanding localized wall deposition. *Protoplasma*. 2002:219(3–4):197–209. https://doi.org/10.1007/s007090200021

Talbot MJ, Wasteneys G, McCurdy DW, Offler CE. Research note: Deposition patterns of cellulose microfibrils in flange wall ingrowths of transfer cells indicate clear parallels with those of secondary wall thickenings. *Funct Plant Biol*. 2007:34(4):307–313. https://doi.org/10.1071/FP06273

Taylor NL, Day DA, Millar AH. Targets of stress-induced oxidative damage in plant mitochondria and their impact on cell carbon/nitrogen metabolism. *J Exp Bot*. 2004:55(394):1–10. https://doi.org/10.1093/jxb/erh001

Tian T, Liu Y, Yan H, You Q, Yi X, Du Z, Xu W, Su Z. agriGO v2.0: a GO analysis toolkit for the agricultural community, 2017 update. *Nucleic Acids Res*. 2017:45(W1):W122–W129. https://doi.org/10.1093/nar/gkx382

Tretter L, Adam-Vizi V. Alpha-ketoglutarate dehydrogenase: a target and generator of oxidative stress. *Philos Trans R Soc Lond B Biol Sci*. 2005:360(1464):2335–2345. https://doi.org/10.1098/rstb.2005.1764

Tripathi D, Oldenburg DJ, Bendich AJ. Oxidative and glycation damage to mitochondrial DNA and plastid DNA during plant development. *Antioxidants (Basel)*. 2023:12(4):891. https://doi.org/10.3390/antiox12040891

Tsukagoshi H, Busch W, Benfey PN. Transcriptional regulation of ROS controls transition from proliferation to differentiation in the root. *Cell*. 2010:143(4):606–616. https://doi.org/10.1016/j.cell.2010.10.020

Villanueva RAM, Chen ZJ. Ggplot2: elegant graphics for data analysis (2nd ed.). *Measurement (Mahwah N J)*. 2019:17:160–167. https://doi.org/10.1080/15366367.2019.1565254

Vojtek AB, Hollenberg SM. Ras-Raf interaction: two-hybrid analysis. *Methods Enzymol*. 1995:255:331–342. https://doi.org/10.1016/S0076-6879(95)55036-4

Walley JW, Sartor RC, Shen Z, Schmitz RJ, Wu KJ, Urich MA, Nery JR, Smith LG, Schnable JC, Ecker JR, et al. Integration of omic networks in a developmental atlas of maize. *Science*. 2016:353(6301):814–818. https://doi.org/10.1126/science.aag1125

Wang Q, Wang M, Chen J, Qi W, Lai J, Ma Z, Song R. *ENB1* encodes a cellulose synthase 5 that directs synthesis of cell wall ingrowths in maize basal endosperm transfer cells. *Plant Cell*. 2021:34(3): 1054–1074. https://doi.org/10.1093/plcell/koab312

Wang SS, Zhang YX, Yang F, Huang ZQ, Tang J, Hu KD, Zhang H. Sulfur dioxide alleviates programmed cell death in barley aleurone by acting as an antioxidant. *PLoS One*. 2017:12(11): e0188289. https://doi.org/10.1371/journal.pone.0188289

Wang Y, Liu J, Zhao H, Lü W, Zhao J, Yang L, Li N, Du X, Ke Y. Human 1A6/DRIM, the homolog of yeast Utp20, functions in the 18S rRNA processing. *Biochim Biophys Acta*. 2007:1773(6):863–868. https://doi.org/10.1016/j.bbamcr.2007.04.002

Wang Z, Chen W, Zhang S, Lu J, Chen R, Fu J, Gu R, Wang G, Wang J, Cui Y. *Dek504* encodes a mitochondrion-targeted E+-type pentatricopeptide repeat protein essential for RNA editing and seed development in maize. *Int J Mol Sci*. 2022:23(5):2513. https://doi.org/10.3390/ijms23052513

Wenzel D, Palladino F, Jedrusik-Bode M. Epigenetics in *C. elegans*: facts and challenges. *Genesis*. 2011:49(8):647–661. https://doi.org/10.1002/dvg.20762

Wiles ET, Selker EU. H3k27 methylation: a promiscuous repressive chromatin mark. *Curr Opin Genet Dev*. 2017:43:31–37. https://doi.org/10.1016/j.gde.2016.11.001

Wittmeyer K, Cui J, Chatterjee D, Lee TF, Tan Q, Xue W, Jiao Y, Wang PH, Gaffoor I, Ware D, et al. The dominant and poorly penetrant phenotypes of maize *Unstable factor for orange1* are caused by DNA methylation changes at a linked transposon. *Plant Cell*. 2018:30(12): 3006–3023. https://doi.org/10.1105/tpc.18.00546

Wu H, Becraft PW, Dannenhoffer JM. Maize endosperm development: tissues, cells, molecular regulation and grain quality improvement. *Front Plant Sci*. 2022:13:852082. https://doi.org/10.3389/fpls.2022.852082

Xia X, Zhang HM, Offler CE, Patrick JW. A structurally specialized uniform wall layer is essential for constructing wall ingrowth papillae in transfer cells. *Front Plant Sci*. 2017:8:2035. https://doi.org/10.3389/fpls.2017.02035

Xia X, Zhang HM, Offler CE, Patrick JW. Enzymes contributing to the hydrogen peroxide signal dynamics that regulate wall labyrinth formation in transfer cells. *J Exp Bot*. 2020:71(1):219–233. https://doi.org/10.1093/jxb/erz443

Xiong W, Wang C, Zhang X, Yang Q, Shao R, Lai J, Du C. Highly interwoven communities of a gene regulatory network unveil topologically important genes for maize seed development. *Plant J*. 2017:92(6):1143–1156. https://doi.org/10.1111/tpj.13750

Ye R, Wang M, Du H, Chhajed S, Koh J, Liu KH, Shin J, Wu Y, Shi L, Xu L, et al. Glucose-driven TOR-FIE-PRC2 signalling controls plant development. *Nature*. 2022:609(7929):986–993. https://doi.org/10.1038/s41586-022-05171-5

Zeng J, Dong Z, Wu H, Tian Z, Zhao Z. Redox regulation of plant stem cell fate. *EMBO J*. 2017:36(19):2844–2855. https://doi.org/10.15252/embj.201695955

Zhan J, Thakare D, Ma C, Lloyd A, Nixon NM, Arakaki AM, Burnett WJ, Logan KO, Wang D, Wang X, et al. RNA sequencing of laser-capture microdissected compartments of the maize kernel identifies regulatory modules associated with endosperm cell differentiation. *Plant Cell*. 2015:27(3):513–531. https://doi.org/10.1105/tpc.114.135657

Zhang H-M, Devine LB, Xia X, Offler CE, Patrick JW. Ethylene and hydrogen peroxide regulate formation of a sterol-enriched domain essential for wall labyrinth assembly in transfer cells. *J Exp Bot*. 2019a:70(5):1469–1482. https://doi.org/10.1093/jxb/erz003

Zhang H-M, Imtiaz MS, Laver DR, McCurdy DW, Offler CE, van Helden DF, Patrick JW. Polarized and persistent Ca^{2+} plumes define loci for formation of wall ingrowth papillae in transfer cells. *J Exp Bot*. 2015:66(5):1179–1190. https://doi.org/10.1093/jxb/eru460

Zhang J, Zhu Q, Yu H, Li L, Zhang G, Chen X, Jiang M, Tan M. Comprehensive analysis of the cadmium tolerance of abscisic acid-, stress- and ripening-induced proteins (ASRs) in maize. *Int J Mol Sci*. 2019b:20(1):133. https://doi.org/10.3390/ijms20010133

Zhang K, Wang F, Liu B, Xu C, He Q, Cheng W, Zhao X, Ding Z, Zhang W, Zhang K, et al. ZmSKS13, a cupredoxin domain-containing protein, is required for maize kernel development via modulation of redox homeostasis. *New Phytol*. 2021:229(4):2163–2178. https://doi.org/10.1111/nph.16988

Zhang YF, Suzuki M, Sun F, Tan BC. The mitochondrion-targeted PENTATRICOPEPTIDE REPEAT78 protein is required for *nad5* mature mRNA stability and seed development in maize. *Mol Plant*. 2017:10(10):1321–1333. https://doi.org/10.1016/j.molp.2017.09.009

Zhou P, Li Z, Magnusson E, Gomez Cano F, Crisp PA, Noshay JM, Grotewold E, Hirsch CN, Briggs SP, Springer NM. Meta gene regulatory networks in maize highlight functionally relevant regulatory interactions. *Plant Cell*. 2020:32(5):1377–1396. https://doi.org/10.1105/tpc.20.00080

Zhou Y, Andriunas F, Offler CE, McCurdy DW, Patrick JW. An epidermal-specific ethylene signal cascade regulates trans-differentiation of transfer cells in *Vicia faba* cotyledons. *New Phytol*. 2010:185(4):931–943. https://doi.org/10.1111/j.1469-8137.2009.03136.x

Zhu Y, Weng M, Yang Y, Zhang C, Li Z, Shen WH, Dong A. Arabidopsis homologues of the histone chaperone ASF1 are crucial for chromatin replication and cell proliferation in plant development. *Plant J*. 2011:66(3):443–455. https://doi.org/10.1111/j.1365-313X.2011.04504.x